1-1-2013

Fabrication and Characterization of Compact High Resolution Radiation Detectors Based On 4H-SIC N-Type Epilayer and CDZNTE

Kelvin Juvenal Zavalla Mendoza
University of South Carolina - Columbia

FABRICATION AND CHARACTERIZATION OF COMPACT HIGH RESOLUTION RADIATION DETECTORS BASED ON 4H-SIC N-TYPE EPILAYER AND CDZNTE

by

Kelvin J. Zavalla Mendoza

Bachelor of Telecommunication Engineering
Peruvian University of Applied Sciences, 2010

Bachelor of Science
University of South Carolina, 2011

Submitted in Partial Fulfillment of the Requirements

For the Degree of Master of Science in

Electrical Engineering

College of Engineering and Computing

University of South Carolina

2013

Accepted by:

Krishna C. Mandal, Director of Thesis

Bin Zhang, Reader

Lacy Ford, Vice Provost and Dean of Graduate Studies

DEDICATION

I would like to dedicate this work to the most important persons in my life, my parents. Their love and support helped me to come through.

ACKNOWLEDGEMENTS

I would like to thank my advisor, Dr. Krishna C. Mandal, for giving me the opportunity to work in his group and for giving the support, motivation and guidance throughout my graduate school studies. His enthusiasm and dedication to the semiconductor field inspired me to complete this work.

I would also like to thank my committee members, Dr. Krishna C. Mandal and Dr. Bin Zhang, for taking time to oversee my research and their support of my work.

I would also like to thank Dr. Sandeep K. Chaudhuri for his constant technical support and guidance with the radiation detection theory, experimental set-up, and measurements.

Finally, I would like to thank Mr. Sandip Das, Dr. Ramesh M. Krishna, Mr. Abhinav Mehta, Mr. M. A. Mannan, and all my colleagues and friends who directly or indirectly have been part of the process to fulfill this thesis.

ABSTRACT

The need of room-temperature, compact, and high resolution radiation detectors has opened the path for the development of new materials with suitable properties. Silicon carbide (SiC) and CdZnTe (CZT) are semiconductor materials with wide band gap that can operate efficiently at room temperatures (RT) and above. CZT has a high average atomic number (Z) which offers a high photoelectric absorption coefficient for x-/gamma rays. SiC allows high energy heavy ion detection due to its high radiation hardness even at temperatures much higher than room temperatures (RT). This thesis focuses on the fabrication and characterization of semiconductor based radiation detectors for alpha particles and gamma rays and development of various software codes (based on Matlab) required to derive important device parameters from the experimental results in order to improve the device performance further. Characterization includes electrical (I-V and C-V) and spectroscopic (alpha particles and gamma rays) techniques.

Silicon carbide is a semiconductor material suitable for radiation detection at room-temperature and above, and in high radiation field environment due to its wide band gap (3.27 eV at 300 K), high breakdown field, and extremely high radiation hardness. In the present work, Schottky barrier detectors have been fabricated on high quality n-type 4H-SiC epitaxial layer grown on n-type 4H-SiC bulk substrate. The application of epitaxial layer allows to obtain high crystallinity, which is desirable for better charge transport properties. The detectors have been fabricated on 8x8 mm^2 4H-SiC 4° off-cut samples by depositing 10 nm thick nickel contacts (~11 mm^2 of area). Current-voltage (I-V) and

capacitance-voltage (C-V) are measured to investigate the Schottky barrier properties. The I-V characteristics revealed an extremely low leakage current of the order of few pA at high operating reverse biases. Using a thermionic emission model, large Schottky barrier heights of the order of 1.6 eV were calculated. Alpha spectroscopic measurements were conducted using a ^{241}Am radiation source (5.48 MeV) to investigate the charge collection efficiency (CCE) and energy resolution. The spectroscopic measurements revealed very high energy resolution (~0.37% at 5.48 MeV) and minority carrier diffusion length of ~13.2 μm were calculated using a Matlab program developed on the basis of a drift-diffusion model. Electronic noise analyses in terms of equivalent noise charge (ENC) were performed to determine the effect of different noise components that contribute to the total electronic noise in the detection system. A least square fitting algorithm was implemented in Matlab in order to execute these analyses.

For gamma ray detection application, there are certain requirements that the material should fulfill in order to fabricate an efficient detector. $Cd_{0.9}Zn_{0.1}Te$ (CZT) is a high Z compound semiconductor material with convenient properties for gamma ray detection. CZT presents a very high gamma ray absorption coefficient, very low leakage current due to high resistivity, wide band gap (≥1.5 eV at 300K), and high density. The fabrication of the detector involved different steps of polishing and passivation of the surfaces. Electrical contacts were fabricated with gold deposition by DC sputtering, which produced good Ohmic contact. Current-voltage (I-V) characterization was conducted to study the behavior of the contact and to calculate the resistivity of the samples. Gamma ray spectroscopic measurements were performed by using ^{137}Cs radiation source of 662 keV of energy. Digital data were collected and analyzed offline in order to generate

biparametric plots. In general, the performance of CZT detectors is limited by the poor hole transport properties and the presence of various macroscopic and microstructural defects within the crystal, leading to charge trapping or loss. Methods have been developed to compensate for charge trapping by applying offline correction schemes to digitally obtained pulse-height spectra. Biparametric correlation based correction is one such scheme developed in this thesis in which the pulse-heights from the same energy events are correlated to their corresponding depth of interaction and any discrepancies are taken care of by applying suitable correction factor. A Matlab based software was developed in order to apply a correction scheme to the biparametric plots and to improve the results acquired from the detector.

TABLE OF CONTENTS

LIST OF TABLES

LIST OF FIGURES

CHAPTER 1: GENERAL INTRODUCTION

1.1 INTRODUCTION

Radiation is the transmitted energy given by matter in the form of waves (rays) or stream of particles (high-speed particles) and it is present everywhere in our environment. Depending on how they interact with matter, radiation can be characterized as non-ionizing and ionizing radiation. Non-ionizing radiation can deposit energy in the irradiated material, however, it is not enough to remove electrons from their respective atoms. On the other hand, ionizing radiation contains much higher energy which is sufficient to remove electrons from an atom. Ionizing radiations along with suitable radiation detectors can be used or applied to various fields such as medical imaging, Homeland security, space applications, nuclear power plants, etc.

In order to accurately acquire the relevant information from a radiation source, semiconductor materials are used to design radiation detectors due to their unique properties which are absent in gas or liquid detectors. Semiconductor materials can absorb the ionizing radiation (such as gamma rays and alpha particles) emitted from radioactive materials which generate electron-hole pairs. The charge pairs drift under the influence of a bias voltage applied across the semiconductor material and are collected by readout electronics as electronic signals. These signals acquired from the semiconductor material contain the information needed in order to identify radiation activity under a given environment.

Commercially available radiation detectors have been fabricated with semiconductor materials such as silicon (Si) and high-purity germanium (HPGe). However, these materials pose problems related to low band gap energy which translates to high leakage current and need of cooling attachments such as bulky dewars. Also, these conventional detectors exhibit less absorption coefficient from high energy gamma rays. This thesis presents silicon carbide (SiC) and cadmium zinc telluride (CZT) as alternative materials to overcome the previous described problems which can be efficiently used to fabricate room-temperature, compact, and high resolution radiation detectors. Silicon carbide is a semiconductor material suitable for radiation detection at room-temperature and above, and in high radiation field environment due to its wide band gap (3.27 eV at 300 K), high breakdown field, and extremely high radiation hardness. CZT presents a very high gamma ray absorption coefficient, very low leakage current due to high resistivity, wide band gap (≥1.5 eV at 300K), and high atomic density.

1.2 4H-SiC FOR RADIATION DETECTION

There are general characteristics that a semiconductor material should have in order to be a suitable candidate for radiation detection application. Large band gap is a desirable property to achieve low leakage current which helps to achieve low levels of electronic noise. The electron-hole pair creation energy should be low enough to ensure that the ionizing radiation is being absorbed to generate charge pairs. In order to reduce the white series noise, the detector capacitance needs to be low which can be achieved using materials with low dielectric constants. High purity and defect-free materials are desirable in order to have full charge collection by decreasing the charge-trapping effect. High charge carrier mobility and life time values. High atomic displacement energy to prevent

damage in the crystal structure from the incident radiation. High thermal conductivity which allows the detector to work at high temperatures without reducing its properties.

Silicon carbide (SiC) is a suitable material for fabrication of ionizing radiation detectors for high-temperature and high-radiation dose environment where other semiconductors cannot perform properly. SiC allows to eliminate the need of cryogenic cooling attachments making it more compact, light-wight, low power consuming detection systems [1]. SiC is a wide band gap semiconductor material and it can exists in different polytypes. The polytypes of SiC have different stacking sequences of silicon and carbon (Si-C bilayers) where these atoms are coupled together within a planar sheet. There are three well known SiC polytypes: 3C-SiC, 4H-SiC, and 6H-SiC. The number in the polytype nomenclature indicates the frequency of the stacking layer and the letter indicates the structure of the crystal lattice where C and H stand for cubic and hexagonal respectively. Figure 1.1 shows the structure of 4H-SiC where it can be observed that the frequency of the stacking layer repeats every 4 Si-C bilayer.

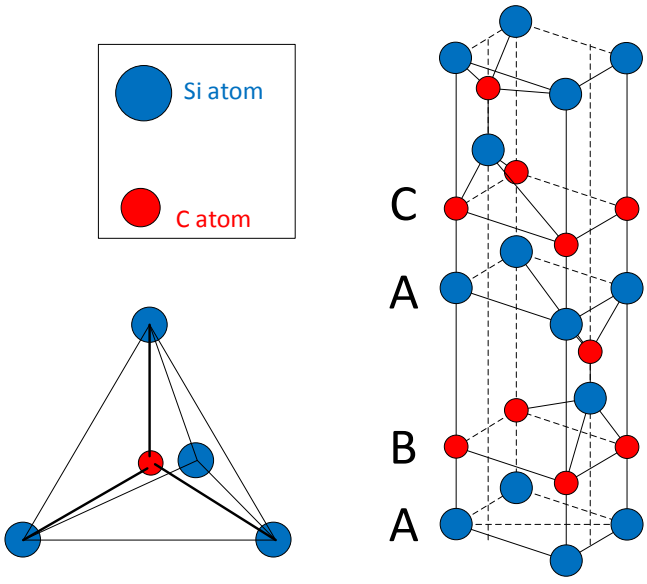

Figure 1.1.The crystal structure of 4H-SiC. Blue spheres are Si and red spheres are C.

The difference in the arrangement of the stacking layers and crystal structure of each polytype assign them different electronic and optical properties. For instance, the band gap at room temperature (300K) for 3C-SiC, 4H-SiC, and 6H-SiC are 2.39 eV, 3.27 and 3.02 eV respectively [1]. Also, other properties like breakdown voltage and saturated drift velocity are unique for each polytypes. As it was described before, large band gap materials are preferable for radiation detection, therefore, 4H-SiC and 6H-SiC can be considered for room-temperature detector fabrication. However, the charge transport properties on 4H-SiC are far more superior to 6H-SiC. Therefore, 4H-SiC is the most appropriate polytype for radiation detection applications.

Table 1.1. Properties of 4H-SiC [1]

Property	4H-SiC
Band gap (eV)	3.27
Electron hole pair creation energy (eV)	7.7
Relative Dielectric Constant	9.7
Electron mobility (cm^2/V.s)	800
Hole mobility (cm^2/V.s)	115
Threshold displacement energy (eV)	22-35

Table 1.1 shows the properties of the polytype 4H-SiC that are relevant for radiation detector fabrication. Low dielectric constant of 4H-SiC compared to Si and Ge helps to reduce the detector capacitance for a given active detector volume, which in turn decreases the white series noise component. The high threshold displacement energy indicates the radiation hardness of the material.

The fabrication of radiation detectors with 4H-SiC generally is based on the growth of higher quality SiC epitaxial layers. SiC epilayers offer high crystallinity, higher growth controllability, and reproducibility compared to its bulk counterpart. Studies using XRD characterization verified the high quality of the 4H-SiC epilayer [2]. However, the presence

of defects in the epilayer and the substrate is one of the crucial factors which limits the performance of the SiC detectors. Major defects present in SiC are edge dislocations, screw dislocations, comet defects, triangular defects, and basal plane dislocations [3] [4] [5]. Most of these defects are normally confined to the substrate [6] but some screw dislocations can propagate to the epitaxial layer and form micropipe defects in the epilayer [7].

The prospect of SiC Schottky diodes as alpha particle detectors was first reported by Babcock and Chang [8]. Ruddy et al. [9] , reported a resolution of 5.8% (full width at half maxima, FWHM) at a deposited energy of 294 keV and 6.6% (FWHM) at a deposited energy of 260 keV by alpha particles from a collimated ^{238}Pu source in 4H-SiC Schottky diodes with circular contacts of diameter 200 and 400 μm. Nava et al. [10] reported very robust 5.48 MeV alpha particle signal in 4H-SiC epitaxial detectors with circular contacts of ~2 mm diameter. However, they have not achieved a saturation of the charge collection efficiency even at a bias voltage of 200 V. In a later work [11], Ruddy et al. reported an energy resolution of 5.7% for a deposited energy of 89.5 keV alpha particles from a 100 μm collimated ^{148}Gd source in similar detectors with relatively larger Schottky contact diameter of 2.5, 3.5, 4.5 and 6.0 mm and 10 μm thick epilayer. Among high resolution alpha particle detection reports, Ruddy et al. [12] reported fabrication of alpha particle detectors with aluminum guard ring structures using which they obtained an energy resolution close to 46 keV for alpha particles from a ^{238}Pu source and 41.5 keV for alpha particles from a ^{148}Ga source. In another work, Ruddy et al. [13] reported an energy resolution of 20.6 keV for ^{238}Pu alpha particles and Pullia et al. [14] reported 0.9% energy resolution in the 4.8–5.8 MeV energy range at a temperature of 55 °C using a SiC/GaN detector with a 1000 Å Au entrance window.

1.3 CdZnTe for Radiation Detection

The development of gamma ray detection material faces many challenging problems. The detector should be fabricated with a material that must be able to absorb the gamma ray energy to generate charge pairs with appropriate transport properties enabling the read-out electrodes to acquire the signal containing the information of the incident nuclear radiation.

Gamma ray radiation detection conducted with commercially available detectors based on semiconductor materials like high purity germanium (HPGe), mercuric iodide (HgI_2), and cadmium telluride (CdTe) can pose serious problems under certain circumstances. HPGe has a high atomic number (which help in the gamma ray energy absorption), it can be produced in large volumes, and it has reached to an exceptional energy resolution of 0.2% for 662 keV gamma ray radiation [15]. However, HPGe has a very low band gap of 0.67 eV at 300K [16] which means that it needs to be cryogenically cooled to liquid nitrogen temperatures (~77K) in order to obtain minimum leakage current. HgI_2 has a high atomic number and also a wide band-gap, however the charge carrier transport properties of electrons and holes are very poor [17] which limits its application for gamma ray detection. Furthermore, HgI_2 is a hygroscopic and soft material which requires this material to be hermetically sealed. CdTe has decent carrier transport properties which makes it a suitable candidate for gamma ray radiation detection, however, its band gap has a limit of 1.5 eV at 300K and its typical resistivity is ~10^8-~10^9 Ω-cm [18]. Cadmium zinc telluride (CZT) is presented as an alternative material to overcome the limitations of the materials previously described for gamma ray radiation detection application.

Table 1.2. Physical properties of CdZnTe related to radiation detection.

Property	Value
Band gap	Tunable: 1.5 to 2.2 eV at 300K
Atomic Number	Cd: 48 Zn: 30 Te: 52
Resistivity	$>10^{10}$ Ω-cm
Electron Mobility Lifetime Product ($\mu\tau_e$)	$10^{-2} – 10^{-3}$ cm^2/V
Electron Mobility (μ_e)	>1000 $cm^2/V.s$
Hole Mobility Lifetime Product ($\mu\tau_h$)	~10^{-5} cm^2/V
Hole Mobility (μ_h)	~50 $cm^2/V.s$

CdZnTe is a direct band gap semiconductor material based on cadmium telluride (CdTe) alloyed with zinc. Table 1.2 shows the properties of CZT that are important for fabrication of radiation detectors of gamma ray. CZT has a high band gap at room temperature which facilitates the fabrication process by eliminating the need of liquid nitrogen dewar in the final detector design. The band gap is tunable and can be varied between 1.5 to 2.2 eV by changing the concentration of zinc (x) present in $Cd_{1-x}Zn_xTe$. The constituent elements in CZT (Cd: 48, Zn: 30, and Te: 52) have a high atomic numbers which is important for a detector material to be able to stop and absorb the high energy gamma ray. Its resistivity is high enough to reduce the effect of noise produced by the leakage current. CZT offers decent charge transport properties, especially for electrons. Hole mobility in CZT is comparatively low which can affect the performance of the detector. However there are alternative solutions to compensate for the poor hole transport properties. Table 1.3 shows the properties of CdZnTe in comparison with other common semiconductor materials used for high energy gamma ray detection.

Table 1.3. Physical properties of gamma ray semiconductor detectors at 300K [16].

Properties/Material	Ge	CdTe	$Cd_{0.9}Zn_{0.1}Te$	HgI_2
Crystal Structure	Cubic	Cubic(ZB)	Cubic(ZB)	Tetragonal
Atomic Number	32	48, 52	48, 30, 52	80, 53
Density (g/cm^3)	5.33	6.20	5.78	6.4
Band gap (eV)at 300K	0.67	1.50	1.58	2.13
Electron hole pair creation energy (eV)	2.96	4.43	4.6	4.2
Resistivity (Ω-cm) at 300K	50	10^9	10^{10}	10^{13}
$\mu_e\tau_e$ (cm^2/V)	>1	10^{-3}	$10^{-3} – 10^{-2}$	10^{-4}
$\mu_h\tau_h$ (cm^2/V)	>1	10^{-4}	10^{-5}	10^{-5}

1.4 THESIS OVERVIEW

The present study has three major objectives. The first objective is the fabrication of radiation detectors based on CdZnTe and 4H-SiC for gamma rays and alpha particles respectively. The second objective is electrical and spectroscopic characterization of 4H-SiC epilayer detectors using a ^{241}Am (5.48 MeV) alpha particle source and analysis of the system noise in terms of equivalent noise charge (ENC). The third objective is the electrical and spectroscopic characterization of CZT detectors with different configuration (planar geometry and virtual Frisch grid) using ^{137}Cs (662 keV) gamma ray source, generate biparametric plots and develop and apply correction schemes to improve the detector performance. This thesis is divided into six chapters.

Chapter 1 provides a background and review of 4H-SiC and CZT properties and how these materials are suitable for radiation detection application. Also, a comparison is made between current radiation detection semiconductor materials with CZT.

Chapter 2 describes the theoretical background of the experimental procedures used in this study. The topics discussed in this chapter are metal-semiconductor contacts,

thermionic emission model, doping concentration, and built-in voltage calculations from C-V measurements, radiation interactions with semiconductor materials, drift-diffusion model, virtual Frisch grid detector configuration, and biparametric correlation correction.

Chapter 3 describes the experimental procedures for the techniques used in this thesis. This chapter includes the details of fabrication of 4H-SiC and CZT radiation detectors. The experimental set up for electrical characterization, radiation spectroscopy, and gamma ray digital spectroscopy has also been described.

Chapter 4 provides the results from the electrical measurements and spectroscopic characterizations performed on 4H-SiC Schottky barrier detectors using a ^{241}Am (5.48 MeV) alpha particle radiation source. A thermionic emission model is applied to study the contacts. A drift-diffusion model has been used to study the separate contribution of charge carrier drift and diffusion to the overall charge collection efficiency and to obtain information on minority diffusion length. Electronic noise analysis of the detection system is performed in terms of equivalent noise charge (ENC) in order to derive the contribution of white series noise, pink noise (f parallel and $1/f$ series) and parallel white noise.

Chapter 5 provides the results obtained from the electrical and spectroscopic characterizations performed on CZT detectors using a ^{137}Cs (662 keV) gamma ray source. Biparametric plots are generated in order to study the performance of the detectors and identify problems such as charge loss and poor hole mobility. Application of a correction scheme in order to recover the pulse-height spectra from the previously described problems and improve the detector performance.

Chapter 6 summarizes the contents of the thesis and also discusses about the future work that can be carried out as an extension to the future study.

CHAPTER 2: THEORETICAL BACKGROUND

2.1 INTRODUCTION

This chapter describes the theoretical concepts behind the experimental techniques used in this thesis. For the detector fabrication, it is important to understand how to obtain the desired type of metal-semiconductor contact e.g., Ohmic or Schottky. For Schottky contacts, the thermionic emission model is described in order to study the contacts properties in SiC diodes in terms of the barrier height and the ideality using current-voltage (I-V) measurements. For further characterization of the Schottky contact, calculation procedure of doping concentration and built-in voltage using capacitance-voltage (C-V) measurements were described. Since this thesis focuses on radiation detection using semiconductors, the interaction with the semiconductor material for alpha and gamma has also been described. A drift-diffusion model to calculate the minority carrier diffusion length and various contributions to charge collection efficiency has been described. The theory behind the contribution of various factors to the overall electronic noise in a radiation detection system has been discussed in the lights of equivalent noise charge formalism developed by Bertuccio and Pullia [19]. For the case of gamma rays, the concept behind two methods that increase the performance of the detector are described viz., the concept of virtual Frisch grid configuration and biparametric correlation and correction scheme.

2.2 METAL-SEMICONDUCTOR CONTACT

2.2.1 Ohmic Contact

A metal-semiconductor contact is Ohmic when it does not have a rectifying effect providing current conduction in either directions; metal to semiconductor and vice versa. The junction behaves as a resistor which indicates that the current and the voltage drop across the resistance follow a linear relationship.

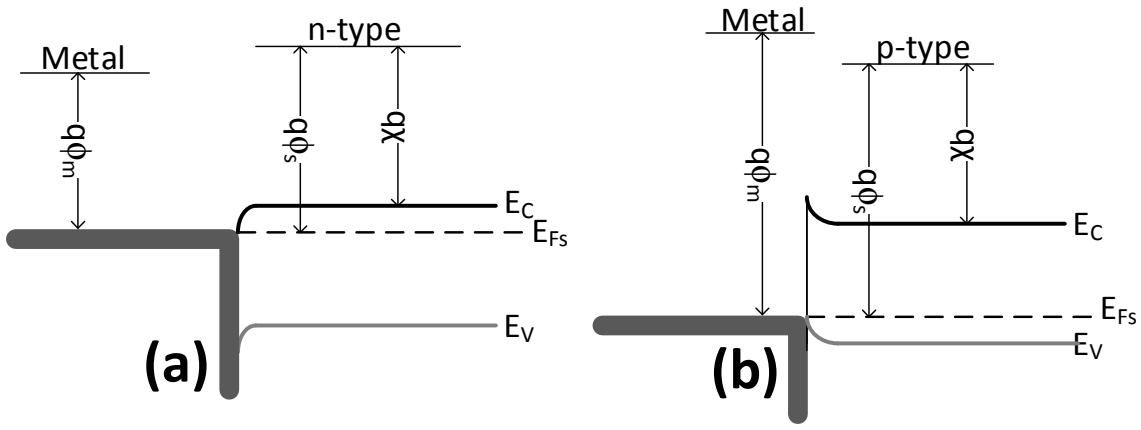

Figure 2.1 Ohmic metal-semiconductor contact energy band diagram after thermal equilibrium. (a) Metal and n-type semiconductor contact. (b) Metal and p-type semiconductor contact.

Figure 2.1 shows an Ohmic metal-semiconductor contact after thermal equilibrium. In both cases it can observed that the Fermi levels are aligned between the metal and the semiconductor. This alignment is achieved because at the moment of forming the junction, the difference between the Fermi levels produces a limited charge exchange at the edges of the bands which leads to the equilibrium of the Fermi levels. The energy band diagrams shows that there is not any barrier that blocks the flow of electrons in the case of metal n-type contact and holes in the case of metal p-type contact, which indicates the presence of current flow through the junction regardless of the polarity of the applied voltage.

The CZT material used for detector fabrication can be considered as intrinsic with the energy band gap of ~1.6 eV at 300K [17] and the electron affinity ~4.3 eV [20]. Work function was calculated to be 5.1 eV using Equation 2.1

$$\phi_s = \chi + \frac{E_g}{2} \qquad 2.1$$

where χ is the electron affinity and E_g is the band gap. In order to form Ohmic contact, deposited metal work function should be higher than 5.1 eV. Therefore, gold with work function of ~5.4 eV is an appropriate metal for Ohmic contact for CZT semiconductor material in the absence of electrically active surface states.

As it is going to be described in section 3.3, that for CZT detectors, their very high resistivity Ohmic contacts are sufficient for detector operation at room temperature. Unlike SiC detectors, because of their comparative low resistivity needs blocking contacts in order to limit the flow of intrinsic current.

2.2.2 Schottky Contact

A metal-semiconductor contact is called Schottky contact when it has a rectifying effect providing current conduction at forward bias (metal to semiconductor) and presenting a low saturation current at reverse bias (semiconductor to metal).

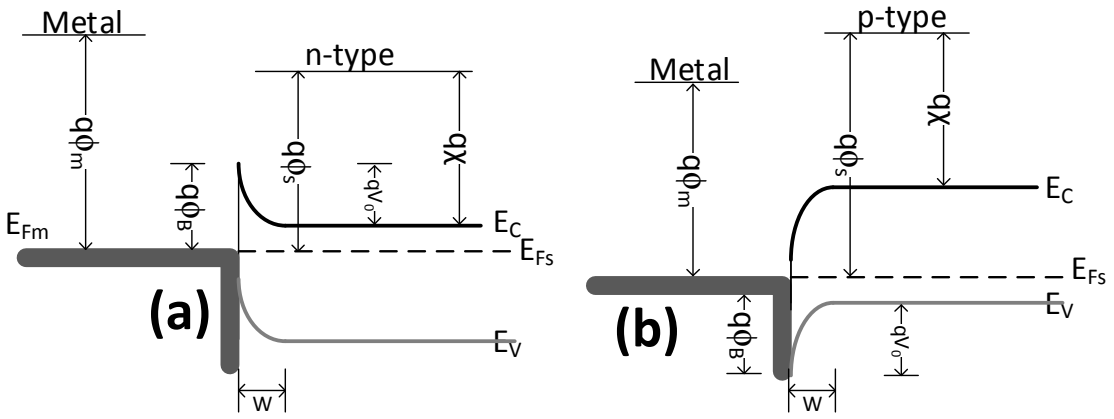

Figure 2.2. Schottky metal-semiconductor energy band diagram after thermal equilibrium. (a) Metal and n-type semiconductor contact. (b) Metal and p-type semiconductor contact.

Figure 2.2 shows the Schottky metal-semiconductor contact after thermal equilibrium. In both cases it can be observed that the Fermi levels are aligned between the metal and the semiconductor. The rectifying effect of the Schottky contact is due to the formation of a barrier height ($q\phi_B$) at the junction which is equal to $q(\phi_m-\chi)$. The built-in voltage (V_0) is obtained from $\phi_m-\phi_s$ (for metal and n-type semiconductor contact) and $\phi_s-\phi_m$ (for metal and p-type semiconductor contact). W is width of the depletion region which is negligible at forward bias, however for reverse bias, it will increase according to Equation 2.2.

$$W = \sqrt{\frac{2 \times V \times \varepsilon \times \varepsilon_0}{q \times N_D}} \qquad 2.2$$

where V is the applied reverse bias, ε is the dielectric constant of semiconductor material, ε_0 is the permittivity of vacuum, q is the electronic charge (1.6×10^{-19} C) and N_D is the effective doping concentration.

Schottky contact barrier height and ideality factor can be analyzed using a thermionic emission model [21], given by Equation 2.3 which relates the forward current to the forward bias in Schottky contact.

$$I = I_s(e^{\frac{\beta V_a}{n}} - 1) \tag{2.3}$$

where I_S is the saturation current, V_a is the applied voltage, n is the diode ideality factor and $\beta = q/k_B T$, q being the electronic charge (1.6×10^{-19} C), k_B the Boltzmann constant (8.62×10^{-5} eV/K), and T is the absolute temperature (°K). The saturation current is given by Equation 2.4.

$$I_S = A^* A T^2 \left(e^{-\beta \varphi_B}\right) \tag{2.4}$$

where A^* is the effective Richardson constant (146 A cm^{-2} K^{-2} for 4H-SiC), A is the area of the diode, φ_B is the Schottky barrier height.

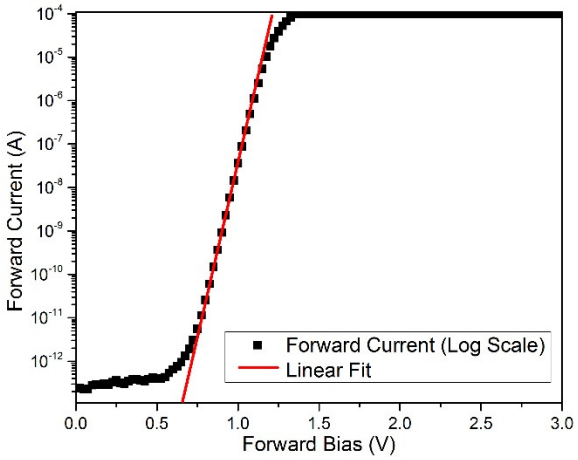

Figure 2.3. Linear fit of current-voltage (I-V) acquired data plotted in logarithmic scale

Equation 2.3 can be written as

$$\log(I) = \frac{\beta V_a}{n} + \log(I_S) \tag{2.5}$$

which is an equation of straight line where $\frac{\beta}{n}$ is the slope and $\log(I_S)$ is the intercept. The slope and the intercept can be easily calculated using a linear regression of log(I) vs V_a plot obtained from I-V measurements. The ideality factor is then obtained from the slope and the barrier height is obtained from the intercept of the equation 2.3. Figure 2.3 shows such a linear fit of an experimental data obtained I-V in a semi logarithmic plot. The diode ideality factor gives the uniformity of surface barrier height across the detector surface [22]. An ideality factor greater than unity, indicates the presence of patches (i.e., presence of generation-recombination centers) on the detector surface where the surface barrier height is considerably lower than the rest of the surface [5].

2.3 Doping concentration and Built-in Voltage Calculation

The effective doping concentration (N_D) in the active region of a detector material can be obtained from C-V measurements in a Schottky or p-n junction diode. The knowledge of effective doping concentration allows the calculation of the depletion width under certain applied bias (shown in Equation 2.2) and also the determination of full depletion bias.

In order to calculate the doping concentration and the built-in voltage, analysis of the data acquired from capacitance-voltage (C-V) measurements is needed.

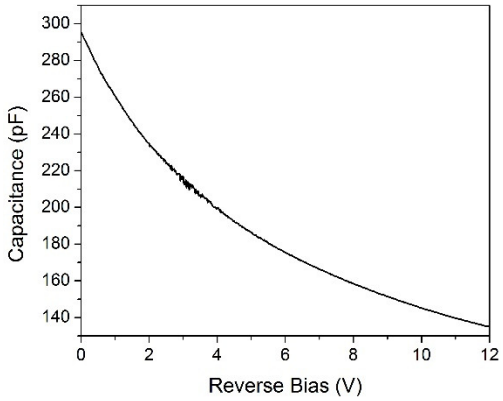

Figure 2.4. Capacitance-voltage data acquired using a 4H-SiC Schottky diode.

Figure 2.4 shows a C-V measurement conducted on a 4H-SiC Schottky device. The capacitance can be seen decreasing with the increase in reverse bias because the capacitance is inversely proportional to the depletion width as is shown in Equation 2.6, and the depletion width in a p-n junction or Schottky diode increases with increase in reverse bias.

$$C = \frac{\varepsilon \times \varepsilon_0 \times A}{W} \tag{2.6}$$

where the symbols have their usual meaning.

The variation of capacitance as a function of reverse bias is given by [23].

$$\frac{1}{C^2} = \frac{2(V_{bi} - \frac{kT}{q})}{A^2 q \varepsilon \varepsilon_0 N_D} - \frac{2(V)}{A^2 q \varepsilon \varepsilon_0 N_D} \tag{2.7}$$

which is a straight line equation in a $1/C^2$ vs. V plot, where the term multiplied to V gives the slope allowing to calculate the doping concentration N_D. The second term of Equation 2.7 allows to calculate the built-in voltage (V_{bi}) using the intercept obtained from the linear fit. Figure 2.5 shows one such linear $1/C^2$ vs. V plot obtained for a 4H-SiC Schottky diode.

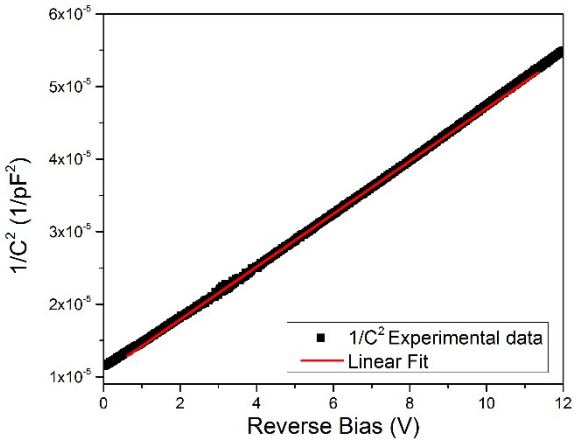

Figure 2.5. $1/C^2$ vs. reverse bias plot with linear fitting. Variation of $1/C^2$ as a function of reverse bias corresponding to the C-V plot shown in Figure 2.4. The straight line shows the linear fit of the experimental data.

2.4 Radiation Interaction with Semiconductor Materials

2.4.1 Alpha Particle Detection

Basically, the interactions of the alpha particles with the absorber matter (detector) create electron hole pairs. Then, an electric field is applied which gives a drift velocity to the free charges generating a current. The radiation signal is obtained from the processing of this generated current. The interaction of alpha particles with matter is mainly due to Coulomb forces between their positive charge and the negative charge of the electrons orbiting within the absorber atoms. Once the charged particle enters the absorbing medium, it interacts simultaneously with many electrons. The attractive Coulomb force generates an impulse on the electron while the particle passes its vicinity. The magnitude of the impulse depends on the proximity of the encounter and this magnitude can be high enough to excite the electrons to a higher energy shell removing them from the atom leading to ionization. The energy absorbed by the electron during the interaction leads to the loss of energy of the alpha particles. If a charged particle of mass m with kinetic energy E interacts with an electron of mass m_0, the maximum transferable energy is $4Em_0/m$ in a single collision.

Continuous interactions with various electrons in the absorber material decreases the velocity of the charge particle until it completely stops. Range in an absorber material is defined as the traversed by the charge particle in that particular material before it loses all its kinetic energy.

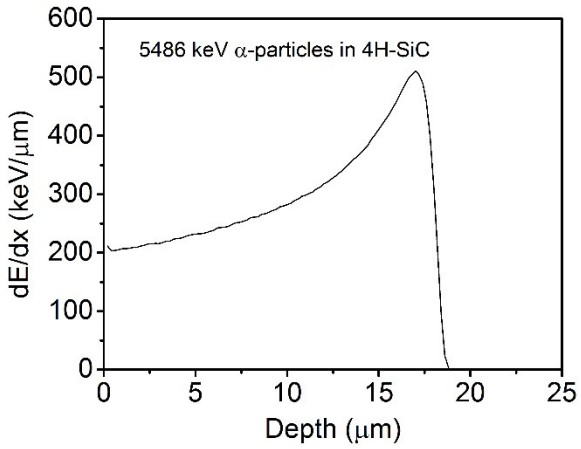

Figure 2.6. Energy loss of 5.48 MeV alpha particle as a function of penetration depth.

Figure 2.6 shows a Bragg curve which shows the energy loss of 5.48 MeV alpha particle as a function of depth of penetration. It can be seen from a Bragg curve that the maximum loss of energy for the alpha particles occurs at the end of the range which is typical of charged particle interaction with matter. [24].

2.4.2 Gamma Ray Detection

The radioactive decay of an unstable atomic nucleus can produce radiation of electromagnetic nature called gamma ray radiation. This radiation usually presents energies higher than 10 keV and it has frequencies higher than 10^{19} Hz. The interaction of the gamma rays and matter can produce charge pairs leading to the generation of electronic current under an applied voltage across the absorbing material. There are three methods of interaction of gamma rays with a matter: photoelectric absorption, Compton scattering, and

electron-positron pair production [24]. It is through these processes that the photon energy of the gamma rays is transformed into electronic energy.

The main mechanism of interaction of gamma ray with matter (detector material) with energies lower than 1 MeV is photoelectric absorption. In this process, an electron in the absorbing material is energized through the interaction with a photon [24]. The energized electron is released from the atom electron shell with energy E_{e^-} given by

$$E_{e-} = hv - E_b \tag{2.8}$$

where E_b is the binding energy of the electron and hv is the photon energy. This ejected electron leaves a vacancy in the electron shell which can be filled by a free electron or a rearrangement of electrons from outer shells causing emission of x-rays. The atomic number of the detector material influences on the photoelectric absorption process because high atomic number increases the probability of interaction of the gamma ray with the material. Therefore, it is recommended to fabricate x/γ-ray detectors with high atomic number materials in order to maximize the probability of photoelectric interaction.

Compton scattering is another type of interaction process between gamma ray and matter. In Compton scattering gamma rays take part in inelastic scattering with electrons [24]. The energy of the scattered gamma ray is shown in Equation 2.9.

$$hv' = \frac{hv}{1 + (\frac{hv}{m_0 C^2})(1 - \cos\theta)} \tag{2.9}$$

where θ is the angle of deflection of the gamma ray, $m_0 C^2$ is the rest mass energy of the electron (0.511 MeV) and hv' is the energy of the scattered gamma ray.

And lastly, pair production is the third interaction process of gamma ray with matter. Unlike the previous processes described before, in this case, the gamma rays have an energy higher than 1.02 MeV (rest mass energy of an electron) which generates an electron-positron pair [24].

2.5 DRIFT-DIFFUSION MODEL

The drift-diffusion model proposed by Breese [25] allows to calculate the minority carrier diffusion length for ion beam induced charge collection measurements. For radiation application, this model is used to calculate the separate contribution of charge carriers produced in the depletion region and that of the diffusion of holes created in the neutral region to the experimentally obtained overall charge collection efficiency (CCE_{obs}). Equation 2.10 describes the concept applied to the model.

$$CCE_{theory} = \frac{1}{E_p}\int_0^d \left(\frac{dE}{dx}\right) dx + \frac{1}{E_p}\int_d^{x_r} \left[\left(\frac{dE}{dx}\right) \times \exp\left\{-\frac{x-d}{L_d}\right\}\right] dx \qquad 2.10$$
$$= CCE_{drift} + CCE_{diffusion}$$

where E_p is the energy of the alpha particles, d is the depletion width at the particular bias, $\frac{dE}{dx}$ is the electronic stopping power of the alpha particles calculated using SRIM 2012 [26], x_r is the projected range of the alpha particles with energy E_p and L_d is the diffusion length of the minority carriers. The first term of the Equation 2.10, CCE_{drift}, gives the contribution of charge generated within the depletion region to the charge collection efficiency and the second term, $CCE_{diffusion}$, is that from the charge carriers created in the region behind the depletion region and diffused to the depletion region.

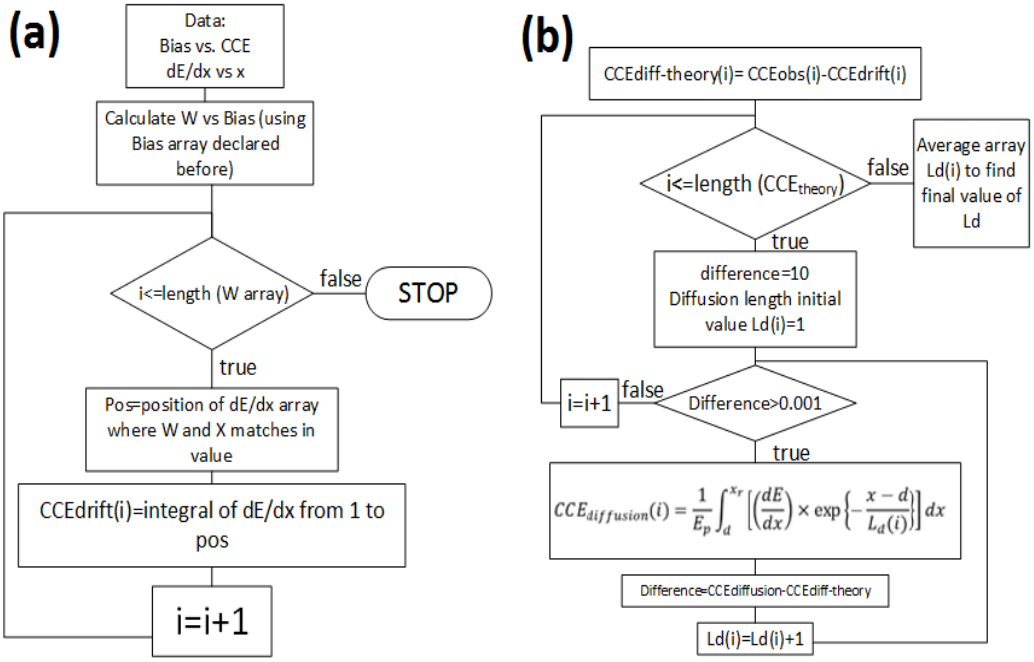

Figure 2.7. Flowchart of the Matlab based code to calculate (a) CCE_{drift}, (b) $CCE_{diffusion}$ and diffusion length L_d.

Figure 2.7(a) shows the flowchart of the developed Matlab based code to calculate the CCE_{drift} (complete code is given in Appendix A). The process started by obtaining the depletion width (W) values as a function of the applied bias. In order to integrate the dE/dx array in terms of dx, it was necessary to find the position of the array where the depletion region (W) and the x array match. This process was repeated for each value of the depletion width and which returned the CCE_{drift} values at a particular bias voltage. Figure 2.9 (b) shows how the $CCE_{diffusion}$ was calculated by using an iteration of CCE_{theory} to CCE_{obs} using L_d as a free parameter.

2.6 Equivalent Noise Charge

In radiation detection application, the current signal generated from the detector usually have a very low magnitude. This signal needs to be amplified in order to be

processed by the detection system. However, the presence of noise sources in the system affects the generated radiation signal compromising the detector performance. This noise can be represented in terms of equivalent noise charge (ENC). Bertuccio and Pullia developed a method shown in Equation 2.11 in order to find the different noise contributions to the ENC and how this process depends on the shaping time of the amplifier [19].

$$ENC^2 = (aC_{tot}^2 A_1)1/\tau + \left[\left(2\pi a_f C_{tot}^2 + b_f/2\pi\right)A_2\right] + (bA_3)\tau \qquad 2.11$$

where τ is the shaping time, A_1, A_2 and A_3 are constants depending on the shaping network response, C_{tot} is the total input capacitance. The parameter a gives the white series noise contribution due to the thermal noise of the FET channel, a_f is the coefficient of the FET $1/f$ noise, b_f is the dieletric noise coefficient and b gives the sum of the white parallel contribution due to the shot noise of the FET and the detector leakage current. The three terms in the right side of Equation 2.11 are the white series noise, pink noise (f parallel and $1/f$ series) and parallel white noise respectively. These terms can be calculated by using a multidimensional least square estimation method where experimental data of three or more values of ENC^2 at different shaping times are available.

2.7 VIRTUAL FRISCH GRID DETECTOR

The virtual Frisch grid detector is a detector structure developed by D. S. McGregor et al. [27] which renders the detector as a single polarity charge carrier (electron) device and helps to get rid of the effects due to poor hole transport properties. Figure 2.8 shows the weighting potential which shows the relationship between the induced charge at the

anode and the depth of interaction. It can be observed that any charge moving from the cathode to the anode does not induce any charge on the anode until it reaches the near grid region. So the charged induced on the anode is free from any movement due to the holes (as long as the interaction is not in the near grid region) and is solely due to movement of electrons in the near grid region.

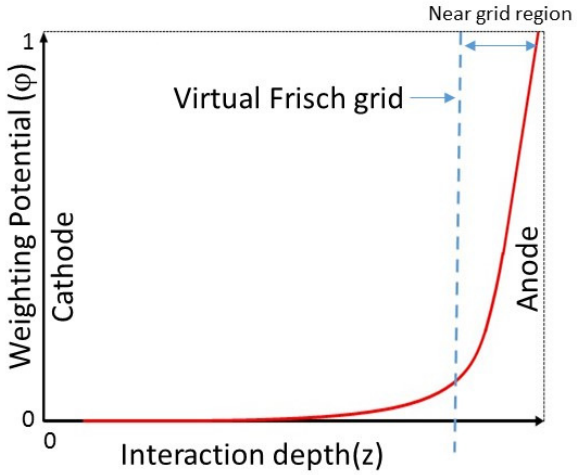

Figure 2.8. Variation of weighting potential as a function of interaction depth in a virtual Frisch grid detector.

2.8 BIPARAMETRIC CORRELATION

Given a random distribution of hole trapping center within the detector thickness and the fact that gamma rays of a particular energy can interact anywhere within the detector thickness, signals with various rise-times and pulse-heights can be obtained for that particular energy. For the interactions close to the cathode, the electron movements form the major part of the signal, but for interactions close to the anode, hole movement contributes more to the signal. Due to their poor transport properties, the holes drift slowly compared to the electrons and hence the resulting signal has a higher rise-time. Finite shaping times in spectroscopic amplifiers may not be sufficient to integrate the entire

charge pulse and obtain the full information i.e., the total charge, leading to an effect called ballistic deficit. Moreover, the holes trapped in defect sites may eventually recombine resulting in a partial charge induction on the anode. Thus, the events for gamma rays with a particular energy may exhibit less pulse-height for interactions close to the cathode. The ballistic deficit and the charge loss cause partial and randomly varying charge collection. This effect is reflected as lower energy event leading to tailing of the full-energy peak at the lower energy side.

The effect of charge loss to pulse-height spectra can be very easily visualized using a biparametric plot. This analysis also allows to study the correlations between pulse height and interaction depth for each gamma event [28]. The process to obtain a biparametric analysis includes digital data acquisition, data processing, and correction. The data acquisition process involves recording digitized pulses from the pre-amplifier. The digitized pulses are shaped using a semi-Gaussian algorithm to filter out the noise required for pulse-height determination. The rise-time was calculated as the time taken for the pre-amplifier pulse height to rise from 10% to 90% of its maximum amplitude. The next step involves generating a frequency table which shows the number of event with a particular set of pulse-height and rise-time. A contour plot (biparametric plot) is generated based on the frequency table which basically shows the frequency distribution of the rise-times and pulse-heights.

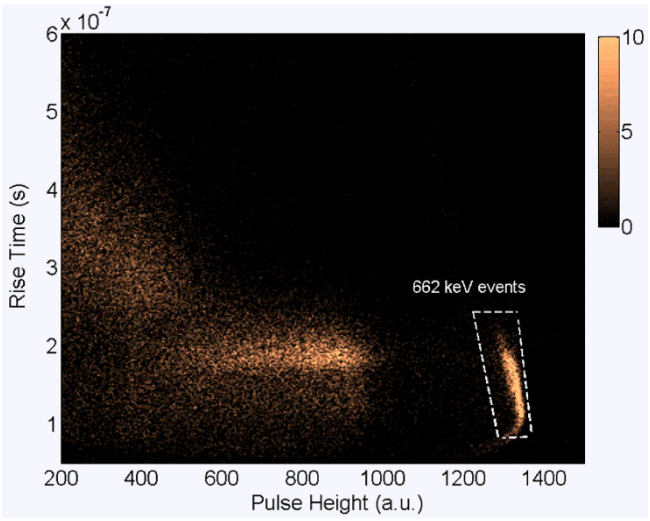

Figure 2.9. Biparametric plot obtained for a CZT detector using a ^{137}Cs source.

Figure 2.9 shows a biparametric plot obtained from a CZT detector using a ^{137}Cs source emitting 662 keV gamma rays. The inclination in the group of events corresponding to the 662 keV interactions as seen in the figure is due to the two effects described previously, ballistic deficit and charge loss. In an ideal case i.e., in the absence of charge trap or loss, these events should appear as a vertically straight band of events. The deviation from the ideal case can be corrected by implementing proper correction schemes which recover the affected events to an improved situation close to the ideal case.

Figure 2.10 shows the biparametric plot shown in Figure 2.11 after the correction applied to the pertinent group of events. In this case, it can be observed that the spectra have been shifted to a position close to the ideal case. The correction scheme was developed based on calculating the distances from the points of interest to a reference which is a line parallel to the rise time axis and corresponding to the position of the unaffected events on the pulse-height axis. Once the distances were calculated, the affected points are shifted to the reference position. The correction scheme only changes the pulse-height (horizontal

change) of the events keeping the rise-time same because any change in the rise-time indicates a different interaction depth which includes inconsistencies between the original and corrected results. As a final step, a pulse height spectrum is regenerated from the corrected pulse-heights in the biparametric plot as will be described in section 5.4.

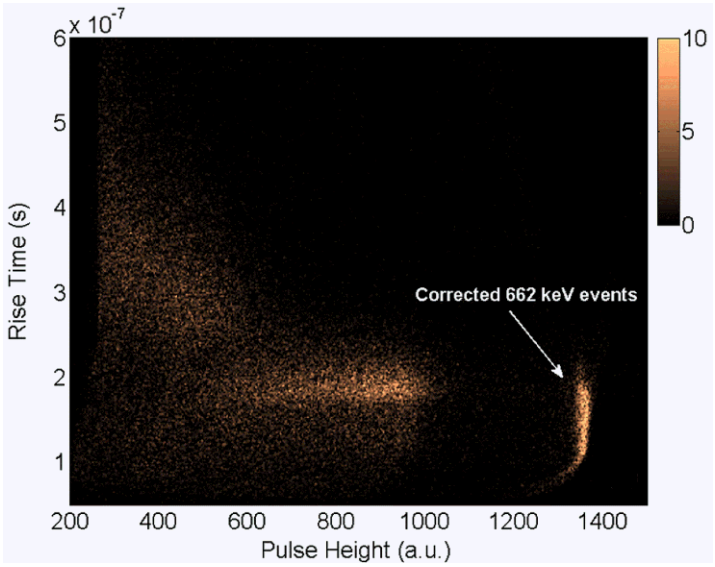

Figure 2.10. Biparametric plot obtained after the application of a correction scheme to the non-ideal biparametric plot shown in Figure 2.9.

CHAPTER 3: EXPERIMENTAL PROCEDURES

3.1 INTRODUCTION

This chapter describes the fabrication and characterization of 4H-SiC and CZT radiation detectors. The fabrication process involves a series of steps depending on the material properties and the type of incident radiation. The performance of a detector greatly depends on the fabrication steps which involve ingot cutting, wafer dicing, cleaning, surface polishing, surface passivation, and metal contact deposition. After the fabrication, the detectors were characterized using current-voltage (I-V) and capacitance-voltage (C-V) measurements. For spectroscopic characterization, pulse-height spectroscopy was carried out using alpha and gamma radiation sources. A digital data acquisition system was set up for implementing a biparametric correction. This chapter also describes the development of various software codes necessary for data acquisition and processing used in this work.

3.2 4H-SIC DETECTOR FABRICATION

The detectors are based on 20 μm thick n-type epitaxial layer, grown on a 4H-SiC (0001) substrate highly doped with nitrogen and 4° off-cut towards the $[11\bar{2}0]$ direction. Nomarski optical microscopy and scanning electron microscopy revealed a micropipe defect density less than 1 cm^{-2}. A 76 mm diameter parent wafer was diced in samples of 8x8 mm^2 as is shown in Figure 3.1.

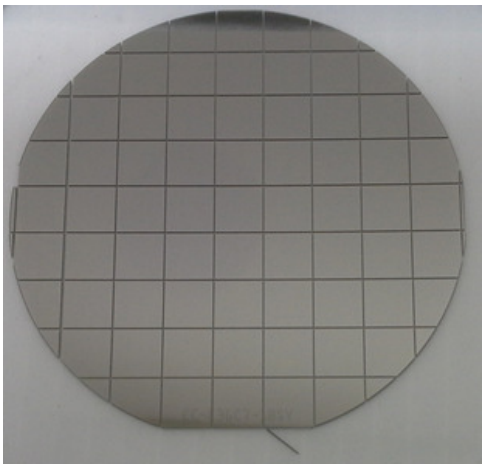

Figure 3.1. Photograph of an n-type 4H-SiC epitaxial layer wafer.

Before contact deposition, RCA standard wafer cleaning procedure was applied. This process starts with the removal of organic contaminants (dust particles, grease, etc.) from the wafer surface by using solvents (trichloroethylene, acetone, and methanol) at a temperature of 70 °C. Any organic residue left by the first step is then processed using sulfuric acid and ammonium hydroxide solutions (with hydrogen peroxide). These solutions are designed to attack the organic impurities by dehydration process and oxidation of the carbon present at the surface of the wafer. Finally, these oxide layers were etched with hydrofluoric acid (HF). Figure 3.2 shows the schematic of the SiC wafer consisting of the 4H-SiC epilayer, 4H-SiC buffer epilayer, and 4H-SiC bulk substrate.

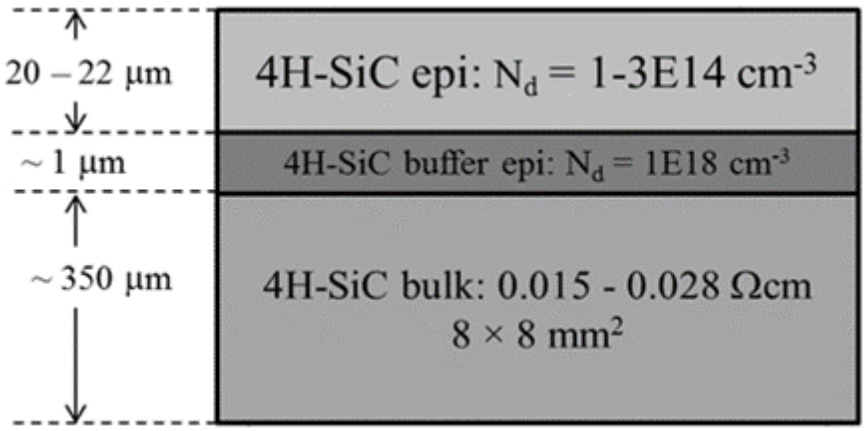

Figure 3.2. Schematic diagram of n-type 4H-SiC epilayer wafer.

Nickel was deposited on the epilayer surfaces to form the Schottky barrier. This deposition was achieved by using a Quorum Q150T DC sputtering unit. The deposited Schottky contact thickness was ~10 nm with an area of ~11 mm^2 (circular shape). Ohmic back contact was achieved by depositing nickel (~100 nm thickness) with an area approximately 6 x 6 mm^2. Figure 3.3 shows a n-type 4H-SiC wafer with Ni deposited on the epilayer face.

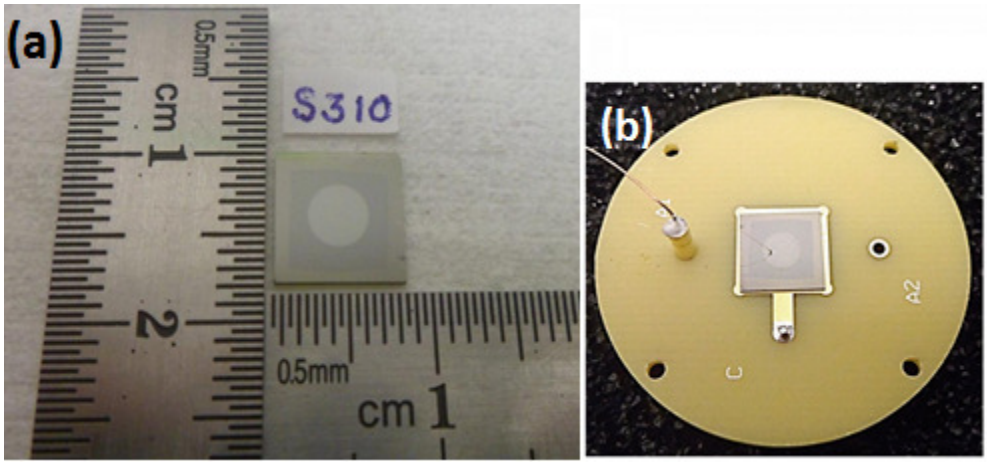

Figure 3.3. (a) Photograph of an actual 4H-SiC epitaxial Schottky barrier detector with nickel contact. (b) A detector mounted on a PCB.

The detectors were then mounted on printed circuit boards (PCB) and wire-bonded for proper electrical connection. The wire-bonding was done using very thin (25 μm) gold wire to ensure less scattering and obscuration of the alpha particles from the wire-bond region. The PCBs were fitted with board-to-board connector pins in order to obtain plug-in modular configuration for stable electrical connections as shown in Figure 3.3 (b).

3.3 CdZnTe Detector Fabrication

Several CZT ingots were grown in our laboratory using a Te solvent method [29] and zone refined precursors [30]. CZT crystals of appropriate sizes have been cut out from the ingot and lapped (down to 1μm SiC paper) and polished (down to 0.05 μm alumina powder). The mechanically polished crystals were etched using a 1.5% Br_2/methanol solution for 60 seconds. In order to reduce the surface leakage currents, passivation of the surface was performed by placing the detector in a Na_2S solution for 15 minutes at a temperature of 60 °C with argon bubbling to prevent oxidation.

Planar and virtual Frisch Grid detection configurations were applied for the detectors fabrication process. First, approximately 70 Å thick gold contacts were deposited on the two opposite surfaces (parallel to (111) crystallographic planes) for electrical contacts using a Quorum Q150T sputtering unit. After the contact deposition step, the planar configuration is completed. However, virtual Frisch grid configuration was achieved with a copper sheath tightly wrapped around the crystal. The length of the copper sheath covered the whole detector thickness. The sheath was electrically insulated from the CZT material by lining the crystal side surfaces with insulating Teflon tape. The insulation reduces the surface leakage current and prohibits leakage current from the sheath. The copper sheath contained a projected tab which was used to connect it to the cathode as the

normal functional configuration of virtual Frisch grid detector needs the cathode and the collar to be equipotential. Finally, these CZT detectors were mounted on PCBs and wire-bonded as described for 4H-SiC detectors (see section 3.2).

3.4 Electrical Characterization

Current-voltage (I-V) and capacitance-voltage (C-V) measurements were conducted, in order to investigate the electrical properties of the metal-semiconductor contact. The I-V measurements were carried out using a Keithley 237 sourcemeter. Forward and reverse bias characteristics were acquired to obtain the behavior of the Schottky contact. C-V measurements were carried out at 100 kHz using a Keithley 590 C-V meter. Figure 3.4 shows the schematic and the arrangement of the system in order to perform the I-V and C-V measurements with the corresponding equipments.

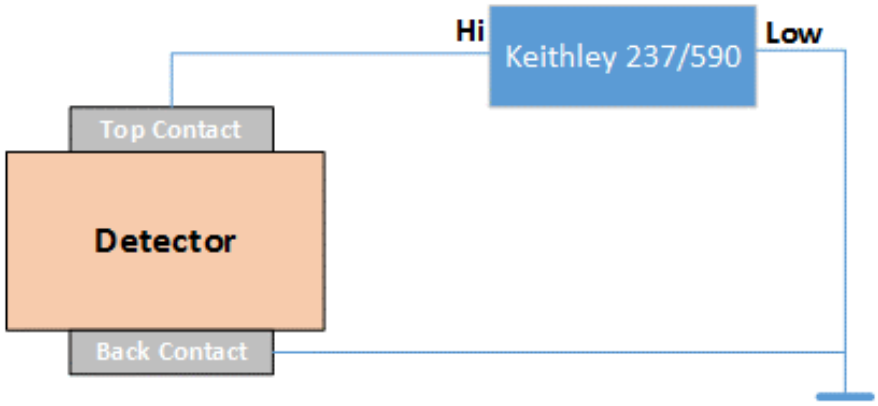

Figure 3.4. Schematic of the experimental set-up for the I-V and C-V measurements.

3.5 Analog Radiation Detection System

Pulse-height spectra of alpha particles were recorded using an analog spectrometer comprised of an Amptek CoolFet (A250CF) preamplifier, an Ortec 572 spectroscopy

amplifier, and a Canberra Multiport II ADC-MCA unit controlled by Genie 2000 interface software. The radiation sources used were 0.1 μCi ^{241}Am alpha source (5.48 MeV) with an active diameter of 7mm and a 0.5μCi ^{137}Cs (667 keV) gamma ray source. The source and the detectors under test were placed inside an RFI/EMI shielded aluminum box.

For alpha particle measurements, the box was constantly evacuated (~10^{-3} mbar) using a rotary pump in order to minimize the scattering of alpha particle with air molecules. The radiation source was placed either illuminating the bottom or the top surface of the detector depending on the specific requirements. Figure 3.5 shows a photograph of the 4H-SiC epitaxial Schottky barrier detector inside RFI/EMI shielded test box.

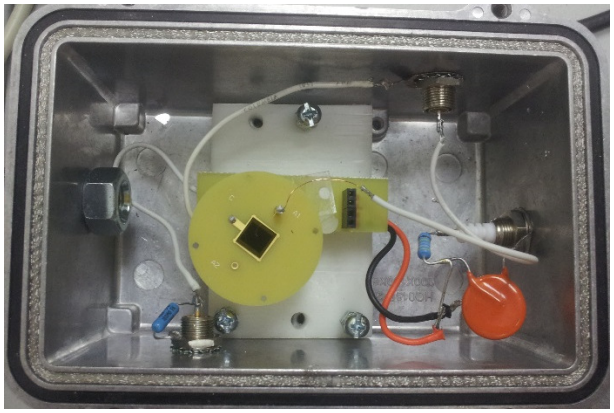

Figure 3.5. Photograph of the 4H-SiC epitaxial Schottky barrier detector inside RFI/EMI shielded test box.

After placing the detectors and the sources in a proper configuration in the test box, the connections between the detector box, the pre-amplifier (A250CF), the NIM modules, the oscilloscope, and the computer were made as shown in Figure 3.6.

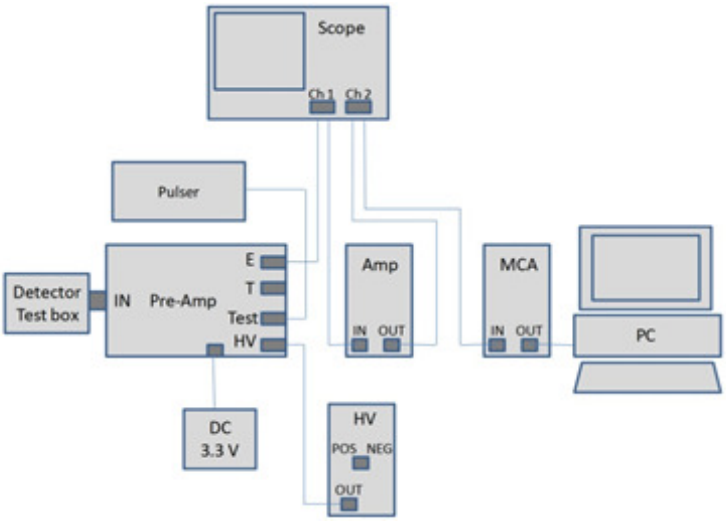

Figure 3.6. Connection schematic for analog data acquisition set-up.

The charges generated in the detector due to the incident radiation energy are collected by the A250CF, which is a charge sensitive low noise pre-amplifier and is best suited for room-temperature detector operation. It hosts a Peltier cooled FET which helps reducing the noise to a great extent. The voltage output of the pre-amp is then fed to an amplifier (Ortec 671) which produces a shaped (semi-Gaussian) amplified output with enhanced signal-to-noise ratio. This is achieved by using a band pass filter consisting of differentiator and integrator circuits. The amplifier allows the user to select the shaping time constant for optimized (trade-off between minimum noise and complete charge collection time) detector performance. This amplified voltage output is directly proportional to the incident energy of the radiation. The amplified output pulse is then fed to a multichannel analyzer (MCA), which basically digitizes the amplifier output pulse signal, and bins the pulses of similar heights in similar bins or channels to obtain a histogram of the distribution of pulse height. The higher is the energy, higher is the channel number. The resulting distribution is called a pulse-height spectrum or simply energy spectrum. The MCA can be calibrated in various ways allowing the user to define each

channel in terms of energy. The software Genie 2000 was used to acquire and save pulse height spectra and also to analyze the acquired data.

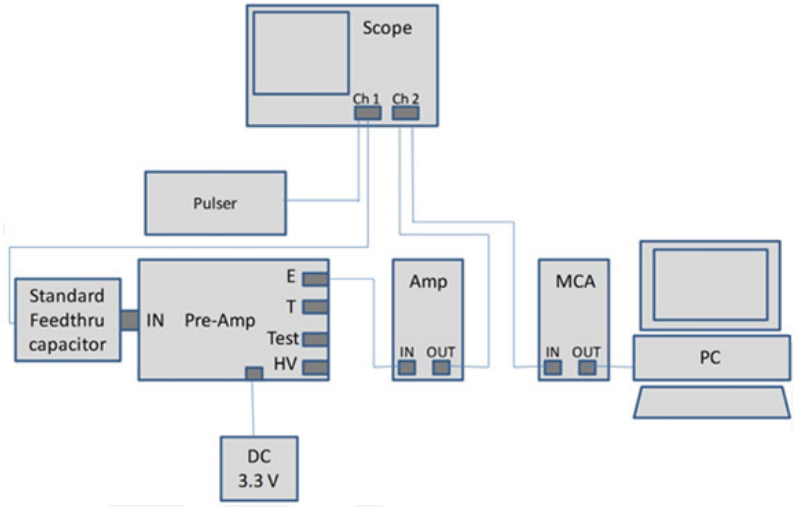

Figure 3.7. Schematic of the electrical connections for energy calibration.

Once the data is acquired, calibration process is performed in order to find a correlation between the channels of the MCA with their corresponding energy. Figure 3.7 shows the connection schematic for energy calibration. It is important to note that the calibration process should be done using the same settings as used in the actual experiment. E_{pulser} in keV was obtained by using Equation 3.1 where ε is the electron-hole pair creation energy (7.7 eV for 4H-SiC and 4.64 eV for CZT [17]).

$$E_{pulser} = \frac{V_{pulser} \times \varepsilon \times C}{1.6 \times 10^{-19}} \qquad 3.1$$

This calibration was accomplished by the injecting pulses of various known amplitudes, V_{pulser} (mV), from a precision pulser (Ortec 419) through a calibrated feed-through capacitor, to the preamplifier input and simultaneously noting down the peak-positions of the shaped pulses in the multi-channel analyzer (MCA). A linear plot of the

peak centroid channel number against the keV equivalent pulser energy gives the required calibration parameters [31].

3.6 Digital Radiation Detection System

Digital data acquisition process was performed for gamma ray radiation detection. In digital data acquisition system, the pre-amplifier pulses generated due to the incident radiation are digitized using a digitizer and stored in a PC for online and offline processing. Figure 3.8 shows the electrical connection arrangement for the digital data acquisition. A NI PCI-5122 digitizer card was used to acquire pulses with a sampling rate of 100 Megasamples per second in real time and with a 14 bit vertical resolution.

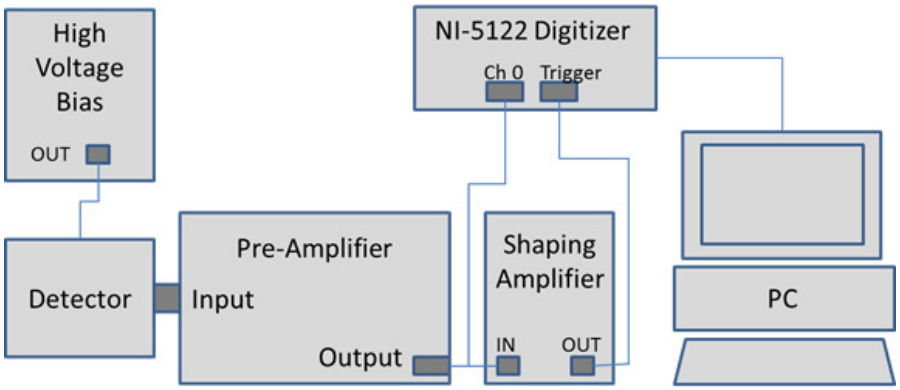

Figure 3.8. Schematics of the electrical connection for digital data acquisition set-up.

A Labview based data-acquisition software was developed to acquire and store the digitized pulses. The data analyses were performed using another program based on Labview and Matlab. These analyses involved digital semi-Gaussian (CR-RC^4) [32] shaping of the pulses followed by pulse-height determination. Biparametric correlation was carried out by mapping the pulse-height of the signal generated from a particular event and the corresponding depth of interaction of that particular event in a 2D graph. The depth of interaction was assumed to be proportional to the rise-time of the pulse. Deviation of the

correlation plots from the ideal behavior can be noticed when there are substantial charge-loss effects associated with the gamma interaction events. Such deviations can be corrected for by incorporating proper correction factors which restores the biparametric plots to a near-ideal situation. Corrected pulse-height spectra were regenerated from the corrected biparametric plots.

CHAPTER 4: 4H-SiC N-TYPE EPITAXIAL LAYER DETECTOR

4.1 INTRODUCTION

This chapter presents the results obtained from the electrical and spectroscopic characterization of the 4H-SiC detectors. Surface barrier detectors were fabricated on 20 μm n-type 4H-SiC epilayers following the procedure described in Chapter 3 section 3.2. The electrical characterization included current-voltage (I-V) and capacitance-voltage (C-V) measurements that helped to determine the Schottky diode behavior e.g. leakage current, barrier-height, ideality factor, and built-in potential. The C-V measurements also helped to determine the effective doping concentration in the epilayer and the variation of the depletion region area with the reverse bias. Alpha spectroscopic characterization was performed to obtain pulse-height spectra to determine the energy resolution of the fabricated detectors. The energy resolution is a conclusive parameter in order to determine the performance of a detector. This chapter also describes the schemes developed to determine the charge transport properties of minority carriers and to study the various electronic components which define the ultimate detector performance.

4.2 ELECTRICAL CHARACTERIZATION

In order to identify the electrical properties of the detectors, I-V and C-V measurements were conducted. I-V characteristics of the detectors at forward and reverse bias were recorded at room temperature. The forward response is used to study the behavior

of the Schottky contacts using the thermionic emission model mentioned in section 2.2 in terms of barrier height and the diode ideality factor. The value of barrier height obtained from forward I–V characteristics is dominated by low Schottky barrier height locations in an inhomogeneous Schottky diode [33]. The reverse I-V characteristics give the magnitude of the leakage current under the operating conditions.

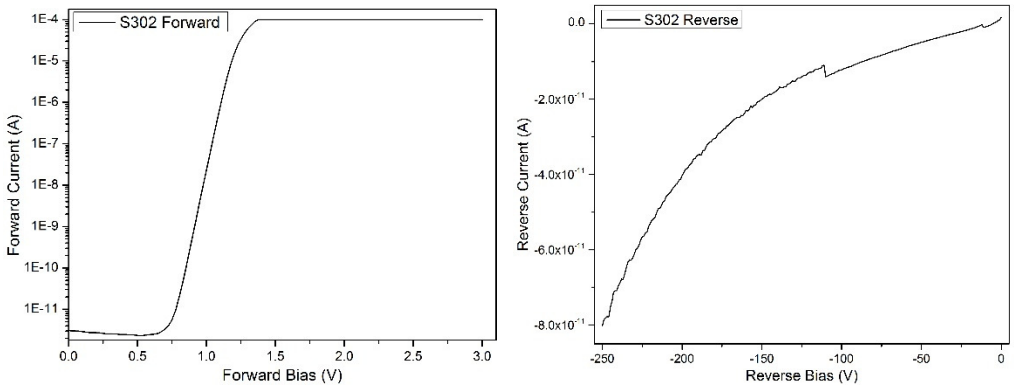

Figure 4.1. Room-temperature I-V characteristics at (a) forward and (b) reverse bias for Schottky barrier detector (S302).

Figure 4.1 shows the results of the I-V measurements for an n-type 4H-SiC Schottky barrier detector S302. The forward response shows a near ideal diode behavior with ideality factor 1.08 and a high surface barrier height of 1.6 eV. A diode ideality factor so close to unity ensures barrier height uniformity across [22] the detector surface and such a high barrier height ensures low leakage current. The reverse bias response accordingly shows low leakage current of 1.84 pA at an operating reverse bias of - 90 V.

Table 4.1. I-V characteristics parameters for good quality Schottky contact.

Diode Name	Current at -90V	Barrier Height (eV)	Ideality Factor
S302	1.84 pA	1.613	1.08

Table 4.1 shows the calculated parameters from the forward and reverse bias response of the detector S302. Such a low leakage current ensures a low parallel noise required for high-resolution detector performance.

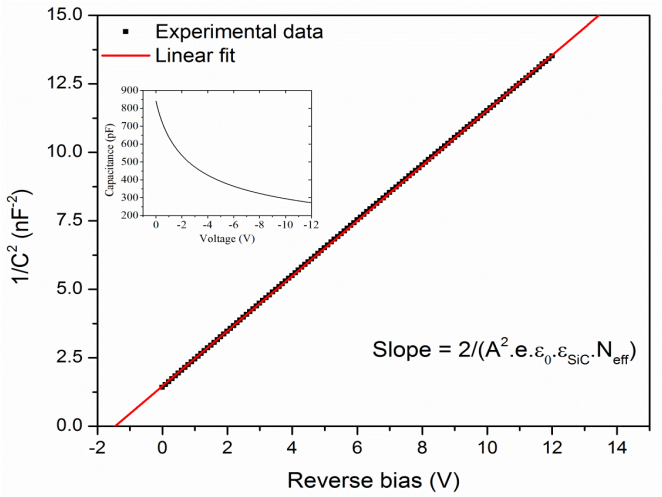

Figure 4.2. $1/C^2$ vs. V plot for n-type 20 µm epitaxial layer 4H-SiC detector. The solid line shows the linear fit to the experimental data. The original C-V plot has been shown in the inset.

Figure 4.2 shows a $1/C^2$ vs V plot and the inset shows the original C-V plot. In a Schottky metal-semiconductor junction, the depletion region extends to the side of the semiconductor and increases its width with the increase in reverse bias. This property allows to control the depletion width in epitaxial layer which defines the active region, the region where the detection of the radiation takes place (creation of electron-hole pairs) of the detector. As the capacitance value depends on the contact area and width of the depletion region, as shown in section 2.3, it is expected to see a decrease in the capacitance value when the reverse bias increases. Further analysis of the acquired data was performed in order to calculate the doping concentration of the epilayer and the built-in voltage of the Schottky contact. As expected, the capacitance values showed a decreasing trend with the increasing reverse bias because of the increase in depletion width. An effective doping

concentration (N_{eff}) of 2.4×10^{14} cm^{-3} was calculated from the slope of the linear fit of the of $1/C^2$ vs V plot where A is the area, e is the electronic charge, ε_0 is the permittivity of vacuum and ε_{SiC} is the dielectric constant of 4H-SiC. Using the calculated value of doping concentration in Equation 4.1, it is possible to calculate the voltage needed in order to fully deplete the detector (thickness of the epilayer). The operating bias needed for full depletion was calculated to be - 90 V for detector S302. It will be shown in the next section that the optimum detector performance was obtained at a bias close to the full depletion width.

$$V = \frac{(W^2 \times e \times N_{eff})}{2 \times \varepsilon \times \varepsilon_0} \qquad 4.1$$

where e is the electronic charge, ε_0 is the permittivity of vacuum, ε is the dielectric constant of 4H-SiC and W is the width of the depletion region.

4.3 Alpha Spectroscopy Measurements

The information obtained by the electrical characterization of the fabricated detectors is useful in order to decide which detectors are suitable for spectroscopic characterization. As discussed in the previous section, the detector S302 is a suitable candidate for radiation detection. Spectroscopic characterization was performed using this detector and a 0.1 μCi ^{241}Am (5.48 MeV) alpha source. The spectrometer was set up following the description in section 3.5.

Figure 4.3 shows the variation of charge collection efficiency (CCE_{obs}) for alpha particles calculated from detector S302 as a function of reverse bias. The CCE_{obs} was calculated as the ratio of the output energy observed by the detector to the actual incident energy of the alpha particles (5.48 MeV). The contribution of the drift ($CCE_{depletion}$) and diffusion ($CCE_{difussion}$) related charge collection to the observed total charge collection

efficiency was calculated using the drift-diffusion model [34] described in section 2.4.1 which was implemented using a Matlab based program.

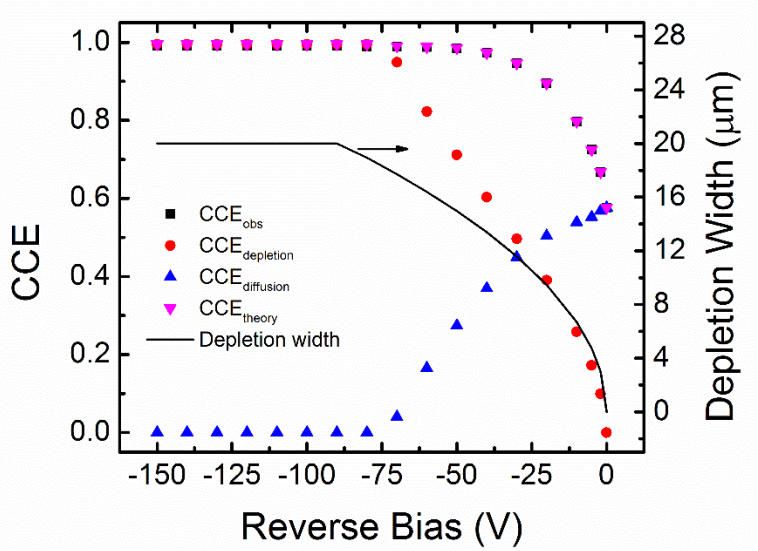

Figure 4.3. Variation of CCE_{obs} and CCE_{theory} as a function of reverse bias voltage. The contributions to the total CCE from charge drifts in depletion region ($CCE_{depletion}$) and from hole diffusion in neutral region ($CCE_{difussion}$) are shown along with the variation of depletion width bias is also shown.

As it can be seen in Figure 4.3, at lower bias voltages, the contribution to the total CCE is mostly dominated by the $CCE_{difussion}$. At lower bias the depletion width was smaller than the alpha penetration depth (~ 18 μm in SiC for 5.486 keV alpha particle), in which case most of the charge carriers were generated in the neutral region and the holes diffuse to the depletion region to get collected. At higher bias, the charge collection efficiency is dominated by the drifting of charge carriers within the depletion width because it becomes comparable or higher than the alpha particle penetration depth Therefore, at a reverse bias beyond -70 V, the $CCE_{depletion}$ values were almost equal to the CCE_{obs} values. The average diffusion length (L_d) was calculated to be ~13.2 μm using the drift-diffusion model and the Matlab code as described in section 2.5. Such a high diffusion length implies the possibility of charge collection even at zero applied bias allowing these detectors to be used without

any applied bias [35]. It can be noticed from Figure 4.3 that at 0V applied bias, the CCE_{obs} is ~40% which indicates how effectively the detector can work by obtaining a robust alpha peak at zero applied bias.

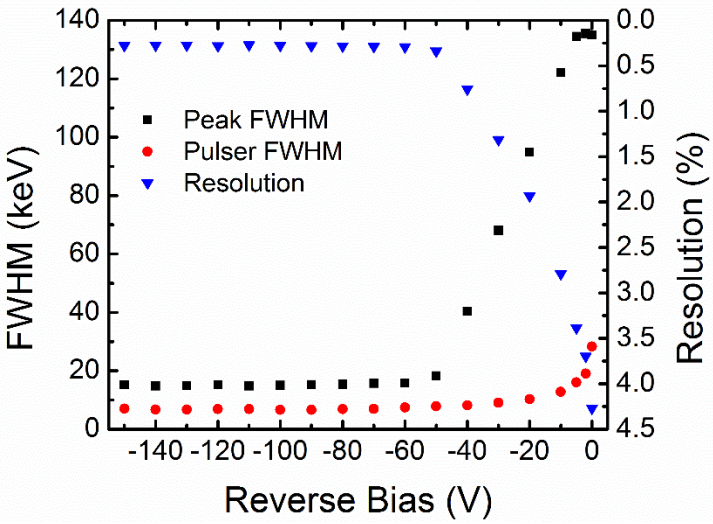

Figure 4.4. Variation of detector resolution as a function of reverse bias. The variation of the pulser peak width is also shown.

Figure 4.4 shows the variation of detector energy resolution (FWHM) in keV and percentage units as a function of reverse bias. The percentage resolution is the ratio between the full-width half-maxima (FWHM) of the peak to the peak centroid. It can be observed that the increment in the bias helped to improve the performance of the detector due to the increased CCE at higher bias. At biases beyond - 70 V, the performance of the detector gets almost saturated, however, experimental results indicated that the best resolution was obtained at - 90 V. Figure 4.4 also shows the variation of the pulser peak width (FWHM) as a function of bias. A systematic initial decrease of FWHM with increasing bias was noticed which indicates the reduction in white series noise and pink

noise as the detector capacitance decreases with increase in reverse bias. The dependence of electronic noise with capacitance is discussed in details in section 4.4.

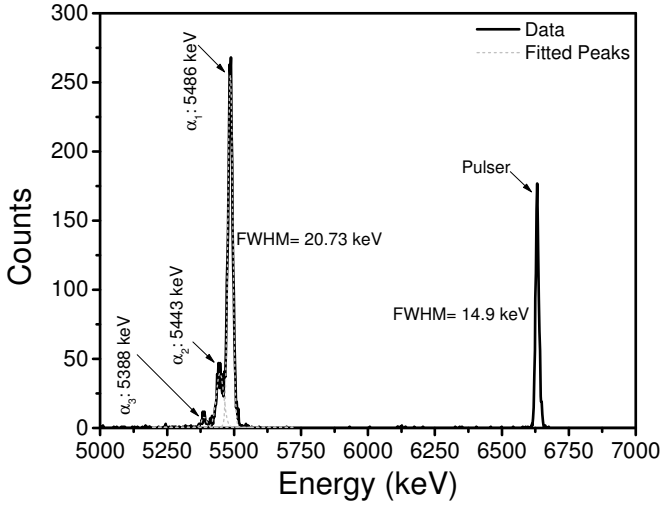

Figure 4.5. Pulse height spectrum obtained using an n-type 4H-SiC epitaxial Schottky detector (S 302) and an ^{241}Am source. A pulser spectrum acquired simultaneously is also shown.

Figure 4.5 shows a pulse-height spectrum acquired using a ^{241}Am source at an optimized operating bias of -90 V and an amplifier shaping time of 3μs. The optimization of the shaping time was carried out by studying the variation of the detector resolution with the amplifier shaping time and will be described in the next section. The pulse-height spectrum in Figure 4.5 shows three clearly resolved alpha peaks. These three peaks correspond to the three major alpha emissions from the ^{241}Am source and their theoretical energies are 5388 keV, 5443 keV, and 5486 keV. The high resolution of the detector allowed to clearly resolving these three peaks with a percentage resolution of 0.37% for the 5486 keV peak. The width of the pulser peak recorded along-with was 7.3 ± 0.2 keV which was less compared to the width observed for the 5486 keV peak (16.2 ± 0.2 keV) implying that the detector performance was not limited by the pre-amplifier noise. The peak width without the broadening due to the electronic noise is defined as the intrinsic

detector resolution which was calculated to be 14.5 keV following a quadrature sum rule [24].

4.4 Equivalent Noise Charge Analysis

As mentioned in the previous section, it is very important to determine the electronic noise and its components as the ultimate detector resolution depends on them. The equivalent noise charge (ENC) is the representation of the contribution of different noise sources that influence in the radiation detection signal acquisition and processing. These noise components were calculated using the formalism developed by Bertuccio and Pullia [19] and has been described in section 2.4.1.

For the ENC measurements, the experimental set up was the same as used for calibration procedure described in section 3.5. The electronic noise was measured from the pulser peak width and expressed in terms of equivalent noise charge (ENC) in charge units as described in section 2.4.1. Pulse-height spectra were acquired using the precission pulser generating pulses at a fixed amplitude and frequency. The pulse-height spectra were recorded as a function of amplifier shaping time. The ENC is plotted as a function of amplifier shaping time τ and fitted to Equation 2.11 using a least square estimation method implemented with Matlab coding as described in section 2.4.1. This program was designed to apply the corresponding fitting to the experimental results in order to calculate the three terms in the right side of Equation 2.11 which are the white series noise, pink noise (f parallel and $1/f$ series) and parallel white noise respectively.

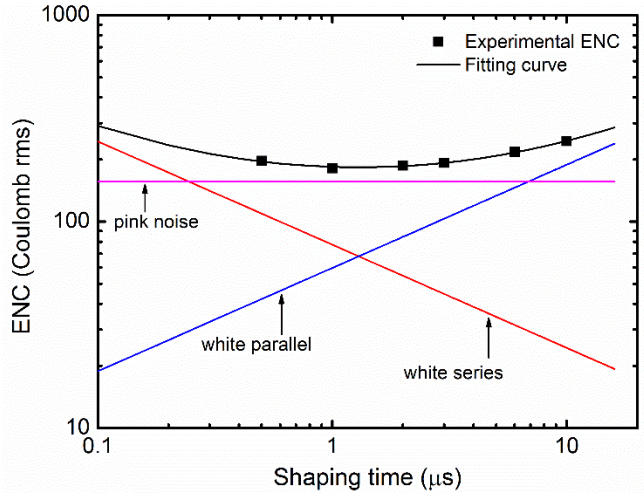

Figure 4.6. Variation of equivalent noise charge as a function of shaping time. The separate contributions from white series noise, white parallel noise, and pink noise are also shown.

Figure 4.6 shows the variation of ENC and various noise contributions calculated as a function of different shaping times. Figure 4.7 shows the same analysis, however, in this particular case, a detector (biased and exposed to the alpha source) is connected to the pre-amplifier. By comparing both the figures, it is possible to see that the ENC is higher when the detector is connected to the system. At any given shaping time, it can be seen from Figure 4.8 that the magnitude of the white parallel noise increased by a factor of ~5 and the white series noise increased by an order of magnitude. The pink noise, which is independent from the shaping time, increased marginally from 156 to 207 Coulomb rms. The white parallel noise increment is due to the additional current from the detector while the increase in white series noise was due to the increase in the input capacitance (detector capacitance was ~55.2 pF at - 90 V). Also, the minimum ENC achievable was different shaping times for the two cases. For Figure 4.6, it can be seen that the minimum ENC was obtained at a shaping time between 1 and 2 μs when the detector was not connected to the

pre-amplifier. However, from Figure 4.7, the minimum ENC was seen to correspond to a shaping time between 3 and 6 μs when the detector was connected to the pre-amplifier.

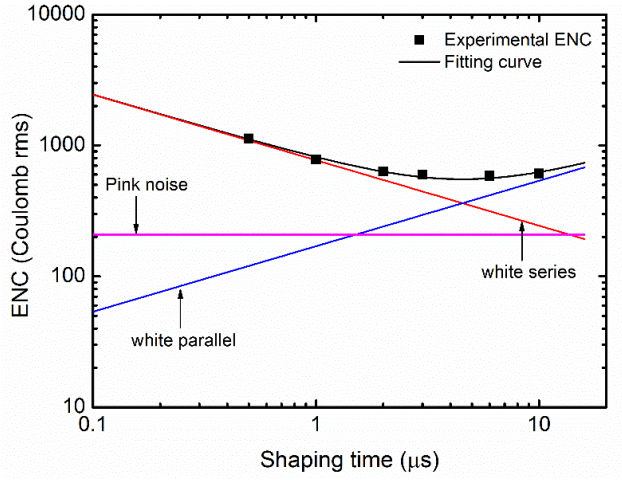

Figure 4.7. Variation of equivalent noise charge as a function of shaping time with S302 detector connected to the pre-amplifier. The detector was biased at - 90 V and exposed to the ^{241}Am source during the measurements.

Figure 4.8 shows dependence of the energy resolution on the shaping time at -90V. It can be observed that the minimum value for resolution corresponds to a 3μs shaping time, which is in accordance with the previous analysis.

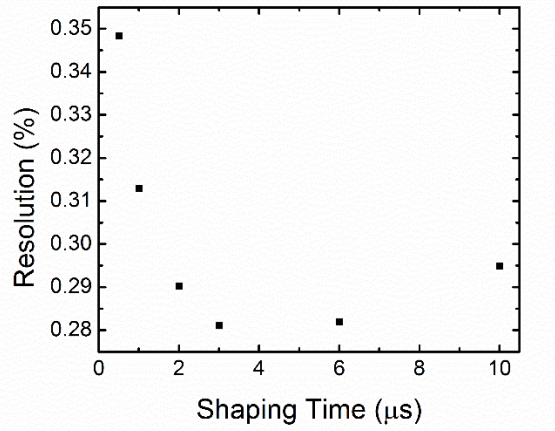

Figure 4.8. Variation of detector resolution as a function of amplifier shaping time measured for 5486 keV alpha particles. The detector was biased at - 90 V.

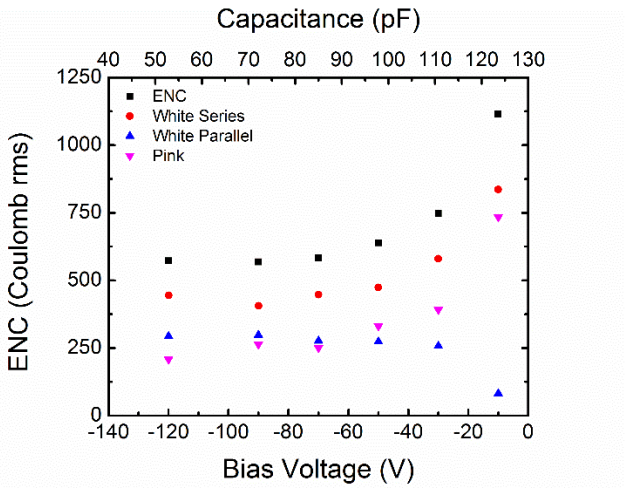

Figure 4.9. Variation of ENC, white series noise and white parallel noise, measured using 3 µs shaping time, as a function of different bias voltages/detector capacitances.

Figure 4.9 shows the variation of ENC and the separate noise contributions to the overall ENC as a function of applied reverse bias and at an optimized shaping time of 3 µs. The detector junction capacitance reduces and the leakage current increases with the applied reverse bias. Also, the contribution of white series noise dominated towards the overall noise and decreases with the increasing reverse bias (or decreasing capacitance). The white parallel noise, that also includes the detector leakage current, was seen to contribute the least at lower biases and increase with reverse bias due to the increase in leakage current. Finally, it can be observed that beyond -50 V bias, the white parallel noise contribution exceeds that of the pink noise.

4.5 CONCLUSION

Electrical and spectroscopic characterizations were performed on 4H-SiC detectors fabricated on 20 µm n-type 4H-SiC epilayers. I-V characteristics revealed the Schottky behavior of the detector (S302). Using a thermionic emission model, the barrier height and diode ideality factor were calculated to be 1.6 eV and 1.08 respectively. The leakage

current at - 90 V was 1.84 pA. Analysis of the C-V measurements revealed a doping concentration of (N_{eff}) of 2.4×10^{14} cm^{-3} and allowed to calculate the bias needed to full depletion of the epilayer which is - 90 V. The electrical characterization results indicated that S302 is suitable for radiation detection. Spectroscopic characterization was performed on S302 detector with ^{241}Am alpha source. A Matlab code was developed to employ a drift-diffusion model which fits the variation of CCE with reverse bias. A diffusion length of ~13.2 μm was calculated using the drift-diffusion model. The percentage energy resolution for 5486 keV peak was found to be 0.37% at - 90V and 3μs of shaping time. Electronic noise in terms of equivalent noise charge (ENC) as a function of shaping time was analyzed. A Matlab code was developed in order to calculate the contribution of each type of noise to the total ENC. The contribution of the white series noise to the overall ENC was found to dominate compared to the white parallel and the pink noise up to a reverse bias of -120 V and decrease steadily with decreasing capacitance. The contribution of pink noise was seen to be more than that of the white parallel noise for bias voltages less than -50 V and beyond which the contribution of white parallel noise became more because of the increased leakage current.

CHAPTER 5: GAMMA SPECTROSCOPY USING CZT DETECTOR AND APPLICATION OF BIPARAMETRIC CORRECTION SCHEME

5.1 INTRODUCTION

$Cd_{0.9}Zn_{0.1}Te$ (CZT) is an excellent material for gamma ray detection and spectroscopy because of its high average atomic number, high density, and high band gap. However, CZT crystals suffer from poor charge transport properties, especially for holes. The adverse effect of poor hole transport properties can be compensated for adopting offline digital correction schemes to digitally acquired radiation interaction data. One such scheme is biparametric correction.

This chapter presents the results obtained from the characterization of CZT gamma radiation detectors. Three detectors were used for the present study: two with virtual Frisch grid (detector D1 and D2) and one in planar detector geometry (detector A) shown in Figure 5.1. Current-voltage (I-V) measurements were conducted to calculate the resistivity of the materials and to observe the magnitude of the leakage current. For spectroscopic characterization a 0.5 μCi ^{137}Cs (662 keV) gamma source was used to obtain gamma pulse-height spectrum. A digital spectrometer was set up to acquire digitized pulses from the detectors. Pulse-height spectra were obtained from the three detectors using an analog and the digital spectrometer. A software code based on Matlab and Labview was developed to implement a biparametric correction scheme to the digitally obtained pulses. A study of

difference of biparametric plots and associated correction scheme between planar and Frisch grid configuration has also been presented.

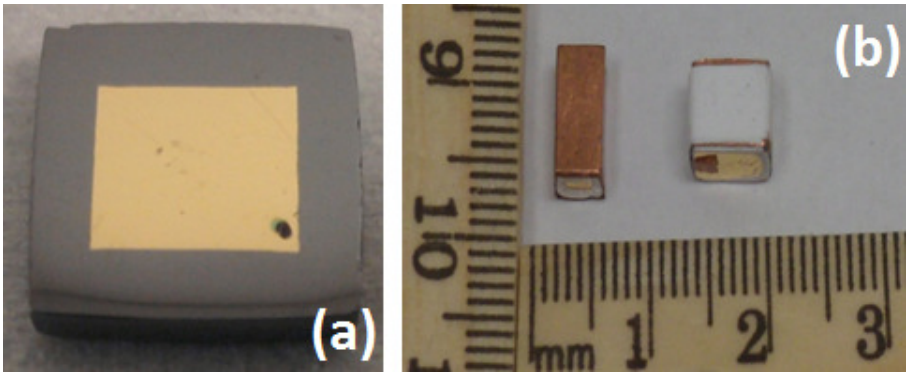

Figure 5.1. Photograph of the three CZT used in the present study. Detectors (a) Planar detector A and (b) Virtual Frisch grid detectors D1 and D2.

5.2 ELECTRICAL CHARACTERIZATION

As it was described in section 3.3, CZT detectors were fabricated with by depositing gold contacts on the two opposite surfaces of CZT single crystals. I-V characteristics were obtained for negative and positive bias in order to verify the contact behavior of the detectors. Resistance of the detectors was calculated from the slope of the linear section of the I-V plot, which is used in Equation 5.1 to calculate the resistivity of the CZT detectors.

$$\rho = R \times \frac{A}{L} \qquad 5.1$$

where R is the resistance of the detector, A is the active contact area and L is the thickness of the detector. Low leakage current and high resistivities are the indicative of good radiation detection.

Figure 5.2(a) shows the I-V characteristics obtained from the planar detector A. It can be observed that there is a distinct asymmetry in the current behavior in the negative and positive bias regime indicating the presence of active deep center at the surfaces which can render the Au/CZT interface as non-Ohmic depending on whether the surface is Cd or

Te rich [36]. The reverse bias response of the detector revealed a current of ~10 nA at -1000 V, while the forward response showed a current of ~1 μA at 500 V. Figure 5.2 (b) shows a low range I-V measurements for resistivity determination. Using Equation 5.1, the bulk resistivity of detector A was calculated to be 6.7×10^{10} Ω-cm.

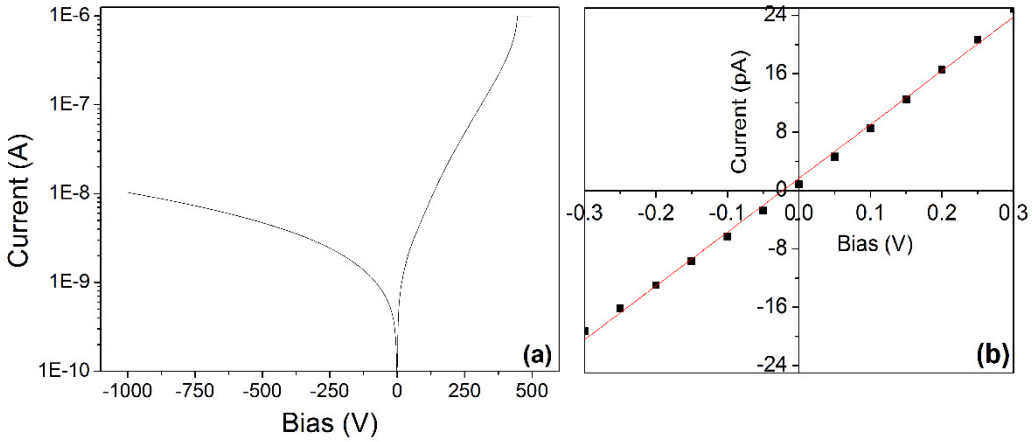

Figure 5.2. (a) I-V curve obtained for CZT crystal A with planar gold contacts. (b) Linear region of the I-V curve for resistivity measurements.

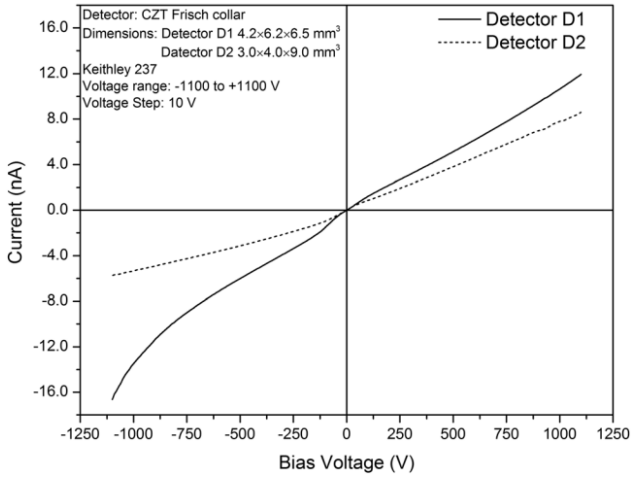

Figure 5.3. Room temperature current-voltage characteristics of detectors D1 and D2 in virtual Frisch grid geometry.

Figure 5.3 shows the results of the I-V measurements for detectors D1 and D2 in virtual Frisch grid geometry. It can be observed that the I-V characteristics were nearly symmetric in the positive and the negative bias ranges, confirming the Ohmic nature of the gold contacts. The response for positive bias revealed a current of ~11 nA for detector D1, and ~8 nA for detector D2 at 1000 V. The magnitude of leakage currents in detector D2 was found to be smaller compared to that in the detector D1 because of its smaller area and larger thickness. Using Equation 5.1, the bulk resistivity obtained for detectors D1 and D2 are 3.42×10^{10} Ω-cm and 1.99×10^{10} Ω-cm respectively. For room temperature nuclear detection application, the desired leakage current in a CZT crystal is achievable when its resistivity is close to ~10^{10} Ω-cm [37] [38]. Therefore, the resistivity values obtained for the present detectors indicate that they are suitable for room temperature radiation detection.

5.3 GAMMA SPECTROSCOPY

Spectroscopic characterization was performed using a 0.5 μCi ^{137}Cs (662 keV) and a 0.1 μCi ^{241}Am (59.5 keV) gamma sources. The measurements were conducted following the description in section 3.6.

Figure 5.4 shows the pulse-height spectrum acquired using a ^{241}Am gamma source and planar detector A biased at 700 V. In a planar detector, the weighting potential or induced charge depends on the depth of radiation interaction. This may render the performance of the detector inefficient because the gamma rays can interact at any arbitrary depth within the detector (particularly for high energy gamma rays). The signal due to the interactions at a considerable depth will be generated by the movement of both electrons

and holes. Since CZT has poor hole transport properties, such signals can considerably affect the detector performance.[241]Am emits low energy gamma rays (59.5 keV) which indicates that the interactions are close to the signal collecting surface. Therefore, the radiation signal produced is mainly due to the movement of electrons under a proper selection of the polarity of the bias. The energy resolution for the planar detector A was calculated for 59.5 keV gamma rays from the pulse-height spectrum shown in Figure 5.4 to be ~7.4%.

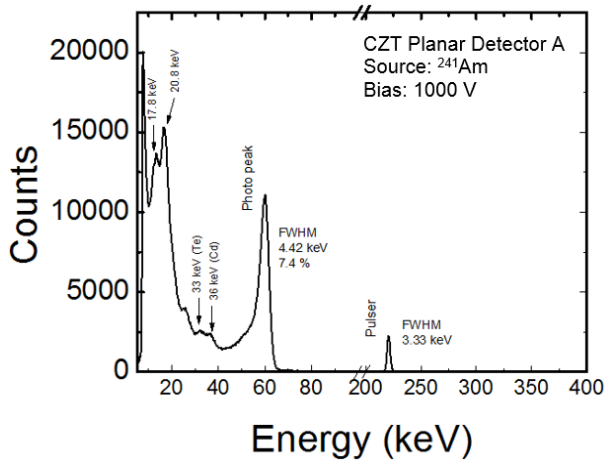

Figure 5.4. Gamma pulse-height spectra obtained using a [241]Am source from planar detector A.

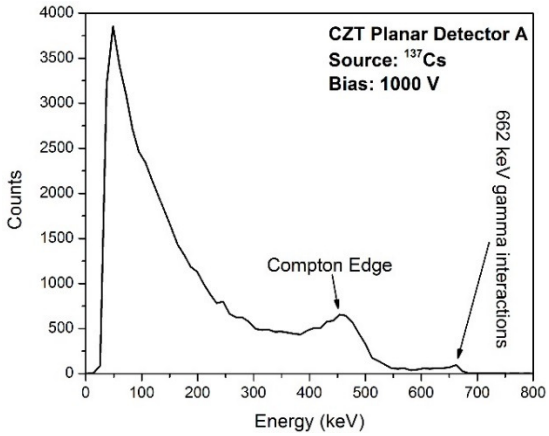

Figure 5.5. Gamma pulse height spectra obtained using a [137]Cs source from planar detector A.

Figure 5.5 shows the pulse-height spectrum acquired using a ^{137}Cs gamma ray source from planar detector A at a bias of 900 V. Since ^{137}Cs is a high energy (662 keV) gamma ray source the interactions primarily occur deep within the detector. Therefore, the detection signals are produced due to the movement of both holes and electrons. This is evident from Figure 5.5 as the prominent spectral features like the full-energy peak, the back scattered peak, etc. were absent in the pulse-height spectrum.

Figure 5.6 shows a ^{241}Am (59.6 keV gamma rays) spectrum obtained using the virtual Frisch grid detectors D1 and D2 biased at 550 V and 1500 V respectively. The percentage energy resolution obtained for detector D1 was 6.1% and for detector D2 is 8.7%. Comparing the performance of planar detector B and Frisch grid detectors D1 and D2, it is possible to observe that the configuration of the detector does not have considerable influence on its performance for detecting low energy gamma rays as far as the energy resolution is concerned.

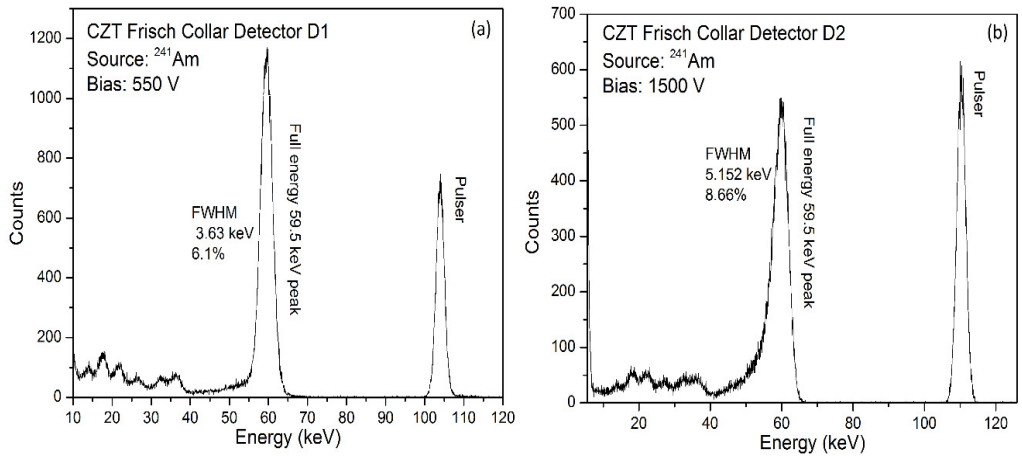

Figure 5.6.^{241}Am spectrum obtained using Frisch grid detector D1 (a) and detector D2 (b) at 550 V and 1500 V bias respectively.

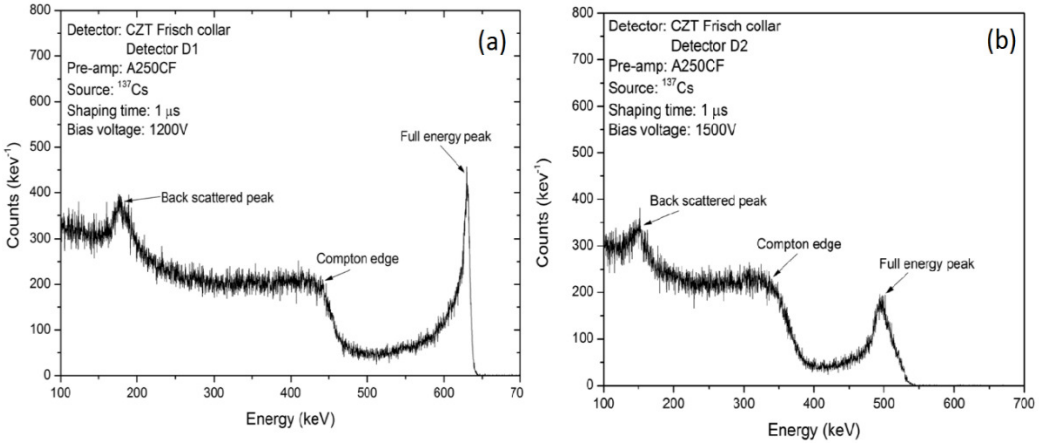

Figure 5.7. ^{137}Cs pulse-height spectrum obtained using Frisch grid detector D1 (a) and detector D2 (b) at 1200 V and 1500 V bias respectively.

Figure 5.7 shows the spectral response of the detector D1 and D2 exposed to ^{137}Cs gamma ray and biased at 1200 V and 1500 V respectively. The full energy peak corresponding to the 662 keV gamma rays was clearly resolved for detector D1. Also, other spectral features like the Compton edge and the backscattered peak were distinctly visible for both detectors. The percentage energy resolution was found to be 1.6% for detector D1 and 5.9% for detector D2. The peak-to-valley ratio (P/V) was 2.6 for detector D1, however, for detector, D2 the P/V value was less than 1. From the spectrum obtained from the detector D2, it can be observed that the full energy peak exhibit much lower energy than 662 keV. Low peak-to-valley ratio and peak-energy mismatch indicate incomplete charge collection due to insufficient strength of the applied electric field or bias. However, increasing the applied bias did not result in improved performance as the leakage current was seen to increase accordingly resulting in increase in parallel noise. It could not be confirmed whether the poor resolution (or poor charge collection) observed for detector D2 is due to the insufficient strength of the electric field or due to the trapping of charges in defect centers.

5.4 BIPARAMETRIC PLOT AND CORRECTION SCHEME

The poor performance of the planar detector A and virtual Frisch grid detector D2 for high energy gamma rays can be recovered using a biparametric correction scheme. In biparametric plots, the pulse-heights from the same energy events are correlated to their corresponding depth of interaction. A biparametric plots is basically a three-dimensional plot with the x-axis representing the pulse-heights, the y-axis representing the rise-time, and the number of events displayed by graded color. Any anomalies in the correlation between pulse-heights and depth of interaction can be identified from a biparametric plot. As has been mentioned in section 2.5, a Matlab based program was developed in order to generate the biparametric plot and to apply the correction scheme.

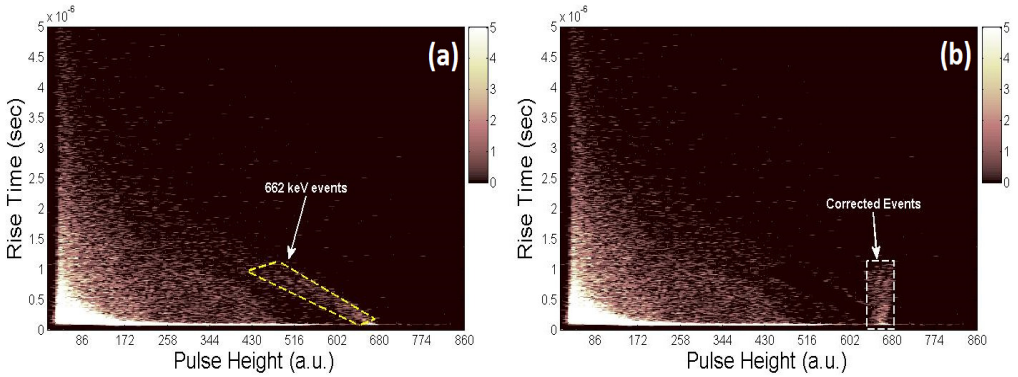

Figure 5.8. Biparametric plot obtained from interaction of 662 keV gamma rays with the planar detector A: (a) uncorrected and (b) corrected.

Figure 5.8(a) shows a biparametric plot generated for the planar detector A irradiated with a ^{137}Cs source. The events within the yellow dotted lines shows the 662 keV photoelectric events. If the detector had been free of charge traps, these events would have appeared as a vertically straight band (parallel to the rise-time axis) of correlated events. However, it can be clearly seen that there is an inclination of the band of the events which in turn indicates that the variation of signal amplitude as a function of depth of interaction

for the 662 keV photoelectric events was affected by charge loss/trapping. In order to recover the pulse-height spectrum from the effect of the hole-trapping, the developed Matlab based correction scheme was applied to the region of interest (yellow lined area). The results of the correction process are shown in Figure 5.8(b) where it can be observed that the 662 keV events appear as vertically straight resembling a charge-trap free detector.

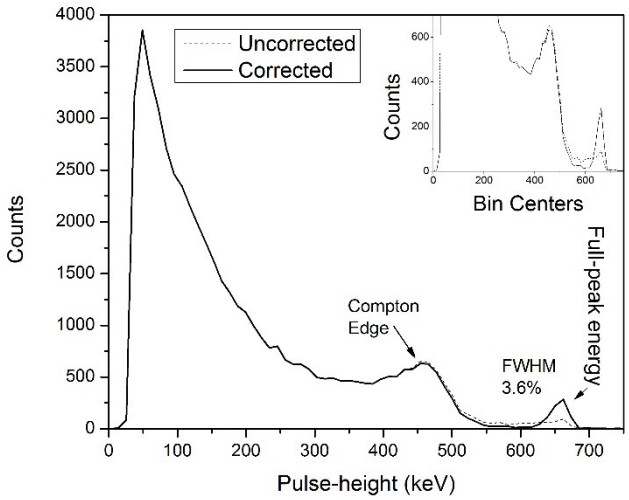

Figure 5.9. ^{137}Cs pulse-height spectrum regenerated after an application of a correction scheme to the biparametric plot shown in Figure 5.8. The dotted lines show the digital pulse-height spectrum obtained before the biparametric correction. The inset shows the magnified region of the 662 keV peak for the corrected and uncorrected spectra.

Figure 5.9 shows the corrected pulse-height spectrum regenerated from the corrected biparametric plot (Figure 5.8). Spectral features like the photo-peak and the Compton edge are clearly visible. A distinct 662 keV peak could be seen in the corrected plot. The percentage energy resolution was calculated to be of 3.6 % for the 662 keV gamma rays.

Figure 5.10 shows the biparametric plot obtained using a ^{137}Cs source for detector D1. The 662 keV full-energy events marked by the dotted lines can be clearly distinguished from the Compton events in the biparametric plot. As has been described earlier, for virtual

Frisch grid detectors, the generated signals are primarily due to the movement of the electrons and that too when they are very close the collection electrode. Hence the generated signals are mostly free from charge trapping effects. It can be observed in the case for detector D1, where the 662 keV events appear as a vertically straight band.

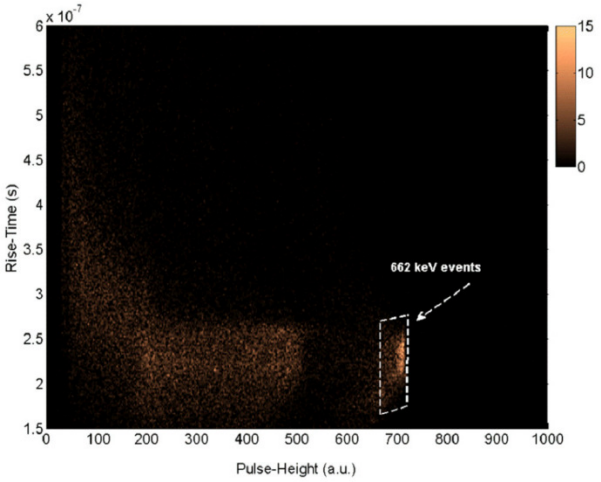

Figure 5.10. Biparametric plot obtained using a ^{137}Cs source for Frisch grid detector D1 [39].

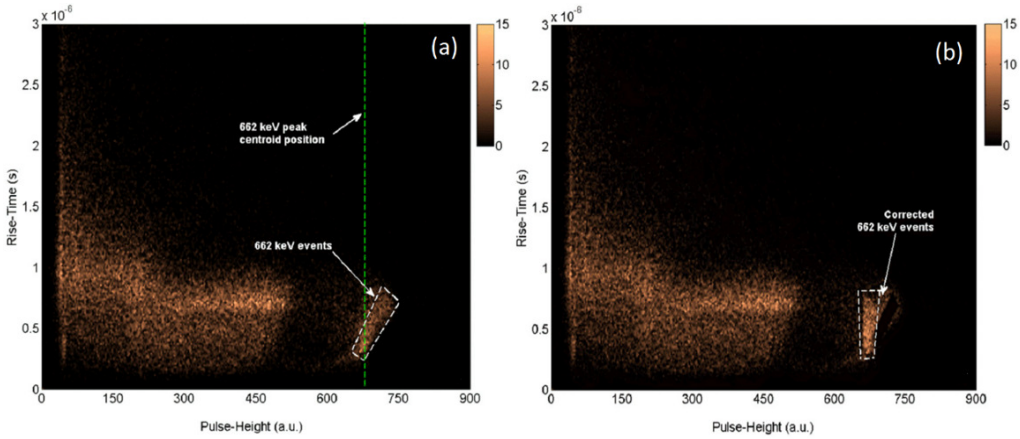

Figure 5.11. Biparametric plot obtained from interaction of 662 keV gamma rays with the planar detector D2: (a) uncorrected and (b) corrected.

On the other hand, Figure 5.11(a) shows a biparametric plot generated for the Frisch grid detector D2 irradiated with ^{137}Cs source. The white dotted lines show the 662 keV photoelectric events. These events were inclined toward the high energy side of the actual

peak position, which is the opposite case from the normal hole trapping effect in planar detector A. This atypical behavior can still be attributed to the hole trapping and de-trapping effect. Figure 5.12 shows two instances of positions of interactions marked as P1 and P2. In the case of interaction at P2, the induced signals would be due to the combined electron-hole movement. The hole current will be affected by their trapping and de-trapping in the detect sites resulting in longer pulse rise-times. On the other hand, for interactions at P1, the output signal will be primarily due to the electron movements. So the induced charge is expected to be less than that of combined charge induction from both electrons and holes and hence shows a lower pulse-height. Since the electron movements are comparatively faster, the rise-times will be smaller for these interactions. This explains why the events with higher rise-time exhibit higher pulse-heights.

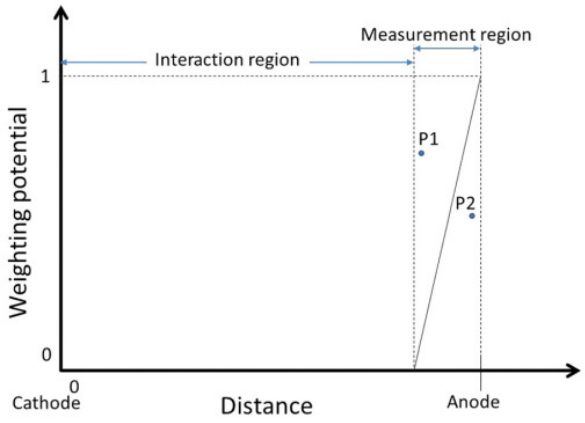

Figure 5.12. Weighting potential distribution in a Frisch grid detector as a function of depth of interaction.

Figure 5.11(b) shows the biparametric plot after applying the developed Matlab based correction scheme to the plot shown in Figure 5.11(a). The positive slope inclined events were selectively aligned to the 662 keV line. The corrected pulse-height spectrum regenerated from the corrected biparametric plot is shown in Figure 5.13. It can be

observed that the photo-peak have a narrower distribution after the correction with a percentage energy resolution of 3.13% for 662 keV gamma rays.

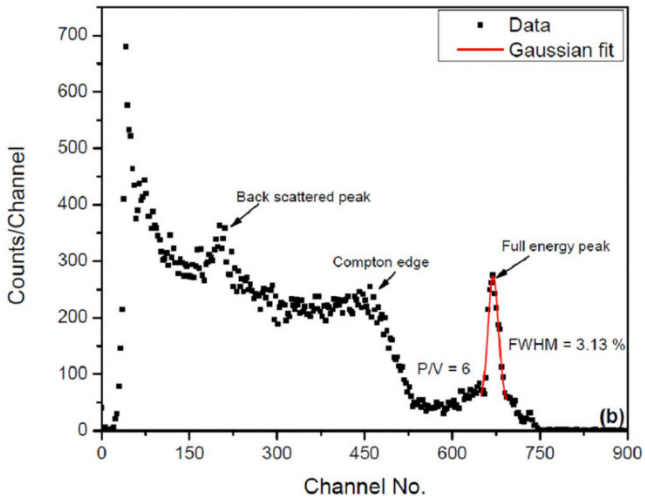

Figure 5.13. ^{137}Cs pulse-height spectrum generated after an application of Matlab based correction scheme to the biparametric plot shown in Figure 5.11(b).

5.5 CONCLUSION

Electrical and spectroscopic characterizations were performed on $Cd_{0.9}Zn_{0.1}Te$ detectors. Three detectors were fabricated: two with virtual Frisch grid (detector D1 and D2) and one with planar detector (detector A) configuration. I-V measurements revealed resistivity greater than 10^{10} Ω-cm. The typical magnitude of leakage current was found to be of the order of few nA at operating voltages. The electrical characterization results indicated that the detectors are suitable for radiation detection. Spectroscopic characterization was performed using a ^{241}Am (59.5 keV) and a ^{137}Cs (662 keV) gamma ray sources. From ^{241}Am gamma pulse-height spectra, the percentage energy resolution of the detectors was found to be 7.4% for detector A, 6.1% for detector D1 and 8.7% for detector D2. From ^{137}Cs gamma pulse-height spectra, the percentage energy resolution of the detectors was calculated to be 1.6% for detector D1 and 5.9% for detector D2. There

was no discernable peak obtained for detector A for 662 keV gamma ray. Biparametric plots were generated from digitally acquired data using the three detectors and the ^{137}Cs gamma ray source. Analyses of these plots revealed that detector A and detector D2 suffer from excessive hole charge trap/loss. A biparametric correction scheme was developed in Matlab to recover the pulse-height spectra. It was observed that the application of the biparametric correction scheme improved the results acquired from the detectors by recovering the pulse-height spectrum from the charge trapping effects.

CHAPTER 6: CONCLUSION AND FUTURE WORK

6.1 CONCLUSION

This thesis is focused on the fabrication and characterization of semiconductor based radiation detectors for alpha particles and gamma rays and development of various software codes (based on Matlab) required to derive important device parameters from the experimental results in order to improve the device performance. Two kind of semiconductor detectors have been chosen for this study viz., epilayer based n-type 4H-SiC detectors for alpha detection and high resistive $Cd_{0.9}Zn_{0.1}Te$ based x/γ-ray detection. The characterization techniques employed to study the detectors are based on electrical measurements which include current and capacitance studies and spectroscopic techniques which involve alpha and gamma detection.

For alpha particle detection, Schottky devices were fabricated on high quality 4H-SiC epitaxial layers. Current-voltage (I-V) and capacitance-voltage (C-V) were measured to investigate the Schottky barrier properties. The I-V characteristics revealed extremely low leakage current of the order of few pA at operating reverse biases close to 100 V. Large Schottky barrier heights of the order of 1.6 eV (calculated by using a thermionic emission model) helped to obtain such low leakage currents. Alpha spectroscopic measurements performed using a ^{241}Am radiation source revealed a percentage energy resolution of ~0.37% for 5486 keV peak. A Matlab based code was developed to fit the experimentally obtained CCE vs bias data to a drift-diffusion model and to calculate the minority carrier diffusion length (L_d). High values of the order of ~13.2μm were calculated for these diodes.

Electronic noise in terms of equivalent noise charge (ENC) as a function of shaping time was analyzed. A Matlab code was developed based on the ENC formalism developed by Bertuccio and Pullia [19] in order to calculate the contribution of each type of noise to the total ENC. The ENC analyses results showed that the electronic noise increased when the detector is plugged in to the pre-amplifier due to the added detector capacitance and leakage current. The measurements also helped to understand that better energy resolution could be obtained by reducing the junction capacitance i.e., by using thicker epilayers.

Gamma ray detectors were fabricated using $Cd_{0.9}Zn_{0.1}Te$ (CZT) single crystal grown in our laboratory using a Te solvent method. CZT is a high Z compound semiconductor material with convenient properties for gamma ray detection. Three detectors were fabricated: two with virtual Frisch grid (detector D1 and D2) and one with planar detector (detector A) configuration. I-V measurements revealed resistivities greater than 10^{10} Ω-cm. The typical magnitude of leakage current was found to be of the order of few tens of nA at operating voltages close to 1000V. Spectroscopic characterizations were performed using an ^{241}Am (59.5 keV) and a ^{137}Cs (662 keV) gamma ray sources. All the detectors irrespective of their configuration showed highly resolved gamma spectra for ^{241}Am low-energy gamma source. For high energy gamma rays (662 keV) both the virtual Frisch grid detectors revealed the 662 keV peak, however the planar detector was found to suffer from the charge loss effects. Biparametric plots were generated from digitally acquired data using the three detectors and the ^{137}Cs gamma ray source. Analyses of these plots confirmed that detector A suffers from excessive hole charge trap/loss. A biparametric correction scheme was developed in Matlab to recover the pulse-height spectra. It was observed that the application of the biparametric correction scheme

improved substantially the results acquired from the detectors by recovering the pulse-height spectrum from the charge trapping effects spectra.

6.2 FUTURE WORK

It has been proven that 4H-SiC epitaxial layer is an excellent material for fabrication of alpha particle detectors due to its high band gap and excellent crystallinity. In order to step forward in the improvement of the detector performance certain additional techniques can be adopted during the detector fabrication process. Passivation of the detector surfaces is one such approach to improve the detector performance by eliminating the effect of the surface states that mediates surface current flow. This process also improves the metal-semiconductor edge interface leading to high break down voltages. Silicon dioxide (SiO_2) and silicon nitride (Si_3N_4) are suitable materials for growing an oxide or nitride layer on SiC which can act as passivating layers. SiO_2 or S_3N_4 can be deposited by plasma-enhanced chemical vapor deposition (PECVD).

It has been studied only two configurations for CZT gamma ray detectors, planar geometry and virtual Frisch grid. However, other types of detector geometries can be investigated such as co-planar, multiple small pixel, and guard-ring.

REFERENCES

[1] F. Nava, G. Bertuccio, A. Cavallini, and A. E. Vittone, "Silicon carbide and its use as a radiation detector material," *Measurement Science and Technology,* vol. 19, pp. 102001-102025, 2008.

[2] K. C. Mandal, P. G. Muzykov, S. K. Chaudhuri and J. R. Terry, "Low Energy X-Ray and γ-Ray Detectors Fabricated on n-Type 4H-SiC Epitaxial Layer," *IEEE Transactions on Nuclear Science,* vol. 60, pp. 2888-2893, 2013.

[3] F. Moscatelli, A. Scorzoni, A. Poggi, M. Bruzzi, S. Sciortino, S. Lagomarsino, G. Wagner, I. Mandic, and R. Nipoti, "Radiation Hardness After Very High Neutron Irradiation of Minimum Ionizing Particle Detectors Based on 4H-SiC p+n Junctions," *IEEE Transactions on Nuclear Science,* vol. 53, no. 3, pp. 1557-1563, 2006.

[4] K. C. Mandal, R. M. Krishna, P. G. Muzykov, S. Das and T. S. Sudarshan, "Characterization of Semi-Insulating 4H Silicon Carbide for Radiation Detectors," *IEEE Transactions on Nuclear Science,* vol. 54, pp. 1992-1999, 2011.

[5] P. G. Muzykov, R. M. Krishna and K. C. Mandal, "Temperature dependence of current conduction in semi-insulating 4H-SiC epitaxial layer," *Applied Physics Letters,* vol. 100, pp. 032101-032105, 2012.

[6] S. Wang, M. Dudley, C. H. Carter Jr. and H. S. Kong, "X-Ray Topographic Studies of Defects in PVT 6H-SiC Substrates and Epitaxial 6H-SiC Thin Films," *Materials Research Society,* vol. 339, pp. 735-740, 1994.

[7] Q. Wahab, A. Ellison, A. Henry, E. Janzén, C. Hallin, J. Di Persio and R. Martinez, "Influence of Epitaxial Growth and Substrate Induced Defects on the Breakdown of High-voltage 4H-SiC Schottky Diodes," *Materials Science Forum,* vol. 338, pp. 1175-1178, 2000.

[8] R. V. Badcock and H. C. Chang, "SiC Neutron Detectors for High Temperature Operation, Neutron Dosimetry," *Proceedings of the Symposium on Neutron Detection, Dosimetry and Standardization,* vol. 1, pp. 613-622, 1962.

[9] H. Ruddy, A. R. Dulloo, J. G. Seidel, S. Seshari and L. B. Rowland, "Development of a Silicon Carbide Radiation Detector," *IEEE Transactinos on Nuclear Science,* vol. 45, pp. 536-541, 1998.

[10] F. Nava, P. Vanni, C. Lanzieri and C. Canali, "Epitaxial silicon carbide charge particle detectors," *Nuclear Instruments and Methods in Phys. Research A,* vol. 437, no. 2-3, pp. 354-358, 1999.

[11] F. Ruddy, A. Dulloo, J. Seidel, J. Palmour and R. Singh, "The charged particle response of silicon carbide semiconductor radiation detectors," *Nuclear Instruments and Methods in Physics Research A,* vol. 505, pp. 159-162, 2003.

[12] F. H. Ruddy, J. G. Seidel, H. Chen, A. R. Dulloo and S.-H. Ryu, "High-Resolution Alpha-Particle Spectrometry Using 4H Silicon Carbide Semiconductor Detectors," *IEEE Transactions on Nuclear Science,* vol. 53, pp. 1713-1718, 2006.

[13] F. Ruddy, J. Seidel and P. Sellin, "High-resolution alpha spectrometry with a thin-window silicon carbide semiconductor detector," *Proceedings of the IEEE Nuclear Science Symposium Conference Record (NSS/MIC),* pp. 2201-2206, 2009.

[14] A. Pullia, G. Bertuccio, D. Maiocchi, S. Caccia and F. Zocca, "An SiC/GaN Detector/Front-End Detection System for High-Resolution Alpha-Particle Spectroscopy," *IEEE Transactions on Nuclear Science,* vol. 55, pp. 3736-3740, 2008.

[15] B. Milbrath, A. Peurrung, M. Bliss and W. Weber, "Radiation detector materials: An overview," *Journal of Materials Research,* vol. 23, pp. 2561-2581, 2008.

[16] S. D. Sordo, L. Abbene, E. Caroli, A. M. Mancini, A. Zappetteni and P. Ubertini, "Progress in the Development of CdTe and CdZnTe Semiconductor Radiation Detectors for Astrophysical and Medical Applications," *Sensors,* vol. 9, pp. 3491-3526, 2009.

[17] A. Owens and A. Peacock, "Compound semiconductor radiation detectors," *Nuclear Instruments and Methods in Physics Research A,* vol. 531, pp. 18-37, 2004.

[18] T. E. Schlesinger and R. B. James, Eds., Semiconductors for Room Temperature Nuclear Detector Applications, San Diego: Academic Press Inc., 1995.

[19] G. Bertuccio and A. Pullia, "A method for the determination of the noise parameters in preamplifying systems for semiconductor radiation detectors," *Reviews of Scientific Instruments ,* vol. 64, pp. 3294-3298, 1993.

[20] S. M. Sze and K. K. Ng, "Metal-Semiconductor Contacts," in *Physics of Semiconductor devices*, Hoboken, New Jersey, John Wiley & Sons, Inc., 2007, pp. 134-190.

[21] E. H. Rhoderick and R. H. Williams, Metal-Semiconductor Contacts, Oxford: Clarendon Press, 1988.

[22] R. T. Tung, "Electron transport at metal-semiconductor interfaces: General theory," *Physical Review B,* vol. 45, pp. 13509-13523, 1992.

[23] B. G. Streetman and S. K. Banerjee, Solid State Electronic Devices, New Jersey: Pearson Education Inc. , 2009.

[24] G. F. Knoll, Radiation Detection and Measurement, 3rd ed., New York: John Wiley & Sons, Inc., 2000.

[25] M. B. H. Breese, "A theory of ion beam induced charge collection," *Journal of Applied Physics,* vol. 74, pp. 3789-3799, 1993.

[26] J. F. Ziegler, J. Biersack and U. Littmark, The Stopping and Range of Ions in Matter, New York: Pergamon Press, 1985.

[27] D. McGregor, R. Rojeski, Z. He, D. Wehe, M. Driver and M. Blakely, "Geometrically weighted semiconductor Frisch grid radiation spectrometers," *Nuclear Instruments and Methods in Physics Research A,* vol. 422, pp. 164-168, 1999.

[28] S. K. Chaudhuri, A. Lohstroh, M. Nakhostin and P. J. Sellin, "Digital pulse height correction in HgI_2 γ-ray detectors," *Journal of Instrumentation,* vol. 7, p. T04002, 2012.

[29] R. M. Krishna, S. K. Chaudhuri, K. J. Zavalla and K. C. Mandal, "Characterization of CdZnTe based virtual Frisch grid detectors for high energy gamma ray detection," *Nuclear Instruments and Methods in Physics Research A,* vol. 701, pp. 208-213, 2013.

[30] S. K. Chaudhuri, R. M. Krishna, K. J. Zavalla, L. Matei, V. Buliga, M. Groza, A. Burger and K. C. Mandal, "$Cd_{0.9}Zn_{0.1}Te$ Crystal Growth and Fabrication of Large Volume Single-Polarity Charge Sensing Gamma Detectors," *IEEE Transactions on Nuclear Science,* vol. 60, pp. 2853-2858, 2013.

[31] S. K. Chaudhuri, K. J. Zavalla and K. C. Mandal, "Experimental determination of electron-hole pair creation energy in 4H-SiC epitaxial layer: An absolute calibration approach," *Applied Physics Letters,* vol. 102, pp. 031109-1-4, 2013.

[32] M. Nakhostin, "Recursive Algorithms for Real-Time Digital CR-$(RC)^n$ Pulse Shaping," *IEEE Transactions on Nuclear Science,* vol. 58, pp. 2378-2381, 2011.

[33] S. K. Chaudhuri, R. M. Krishna, K. J. Zavalla and K. C. Mandal, "Schottky barrier detectors on 4H-SiC n-type epitaxial layer for alpha particles," *Nuclear Instruments and Methods in Physics Research A,* vol. 701, pp. 214-220, 2013.

[34] M. B. H. Breese, A. Saint, F. W. Sexton, K. M. Horn, H. Schone, B. L. Doyle, J. S. Laird and G. J. F. Legge, "Optimization of ionbeam induced charge microscopy for the analysis of the integrated circuits," *Journal of Applied Physics,* vol. 77, pp. 3734-3741, 1995.

[35] S. K. Chaudhuri, K. J. Zavalla and K. C. Mandal, "High Resolution Alpha Particle Detection Using 4H-SiC Epitaxial Layers: Fabrication, Characterization, and Noise Analysis," *Nuclear Instruments and Methods in Physics Research A,* vol. 728, pp. 97-101, 2013.

[36] J. Crocco, H. Bensalah, Q. Zheng, V. Corregidor, E. Avles, A. Castaldini, B. Fraboni, D. Cavalcoli, A. Cavallini, O. Vela and E. Dieguez, "Study of asymmetries of Cd(Zn)Te devices investigated using photo-induced current transient spectroscopy, Rutherford backscattering, surface photo-voltage spectroscopy, and gamma ray spectroscopies," *Journal of Applied Physics,* vol. 112, pp. 074503-1-9, 2012.

[37] T. Schlesinger, J. Toney, H. Yoon, E. Lee, B. Brunett, L. Franks and R. James, "Cadmium zinc telluride and its use as a nuclear radiation detector material," *Materials Science and Engineering,* vol. 32, pp. 103-189, 2001.

[38] A. Burger, H. Chen, K. Chattopadhyay, D. Shi, S. Morgan, W. Collins and R. James, "Characterization of metal contacts on and surfaces of cadmium zinc telluride," *Nuclear Instruments and Methods in Physics Research A,* vol. 428, pp. 8-13, 1999.

[39] S. K. Chaudhuri, K. J. Zavalla, R. M. Krishna and K. C. Mandal, "Biparametric analyses of charge trapping in $Cd_{0.9}Zn_{0.1}Te$ based virtual Frisch grid detectors," *Journal of Applied Physics,* vol. 113, pp. 074504-1-6, 2013.

APPENDIX A - CCE FITTING MATLAB CODE

```
[Bias CCE]=textread('BiasCCE.txt');
[dEdx x]=textread('dedx.txt');
Ep=5.48e3;
Eo=8.854e-12;
Er=9.72;
q=1.6e-19;
Nd=2.4e8;

%Depletion Width
W=sqrt((Eo*Er*2*Bias)/(q*Nd));

for i=1:size(W)
   less=100;
   for j=1:size(x)
      diff= W(i)-x(j);
      pos(1)=1;
     if((diff<less) && (diff>0))
        less=diff;
        pos(i)=j;
      end
   end
   if(pos(i)>1)
      %CCE-Drift
      CCEdrift(i)=(1/Ep)*trapz(x(1:pos(i)),dEdx(1:pos(i)));
   end
end
aux=abs(CCE-CCEdrift');
for i=1:8
   %CCE-Diffusion
   diff=10;
   Lp(i)=1;
  while(diff>0.001)
   CCEdiff(i)=(1/Ep)*trapz(x(pos(i)+1:100),(dEdx(pos(i)+1:100)).*exp(-1*(x(pos(i)+1:100)-W(i))./Lp(i)));
   diff=abs(CCEdiff(i)-aux(i));
   test(i)=diff;
   Lp(i)=Lp(i)+0.01;
  end
end

for i=9:11
   %CCE-Diffusion
   diff=10;
   Lp(i)=1;
  while(diff>0.001)
   CCEdiff(i)=(1/Ep)*trapz(x(pos(i)+1:100),(dEdx(pos(i)+1:100)).*exp(-1*(x(pos(i)+1:100)-
W(14))./Lp(i)));
```

```
    diff=abs(CCEdiff(i)-aux(i));
    test(i)=diff;
    Lp(i)=Lp(i)+0.01;
   end
end
for i=12:16
    %CCE-Diffusion
    diff=10;
    Lp(i)=1;
   while(diff>0.01)
    CCEdiff(i)=(1/Ep)*trapz(x(pos(i)+1:100),(dEdx(pos(i)+1:100)).*exp(-1*(x(pos(i)+1:100)-W(i))./Lp(i)));
    diff=abs(CCEdiff(i)-aux(i));
    test(i)=diff;
    Lp(i)=Lp(i)+0.01;
   end
end

sum=0;
for i=1:8
    sum=sum+Lp(i);
end
% Lp_final=sum/8;
Lp_final=13;

for i=1:size(W)
    CCEdiff_theorical(i)=(1/Ep)*trapz(x(pos(i)+1:100),(dEdx(pos(i)+1:100)).*exp(-1*(x(pos(i)+1:100)-
W(i))./Lp_final));
end

CCE_theorical=CCEdrift+CCEdiff_theorical;
Theorical=CCEdrift+CCEdiff;
```

APPENDIX B - EQUIVALENT NOISE CHARGE CODE

```
close all
clc
clear all

ENC_301_exp=[4810.14217;4869.1327;4487.21357;3669.12171;3148.83733;2486.44549];
ENC_315_0_exp=[3905.15165;4008.18032;2957.65165;2902.62424;2141.7909;1729.11029];
ENC_315_45_exp=[1665.87758;1256.99853;929.01633;817.11307;627.58678;558.84618];
ENC_315_90_exp=[1486.39854;1150.88957;841.59258;700.92777;535.64418;483.90548];
ENC_301=ENC_301_exp.^2;
ENC_315_0=ENC_315_0_exp.^2;
ENC_315_45=ENC_315_45_exp.^2;
ENC_315_90=ENC_315_90_exp.^2;

t=[0.5,1,2,3,6,10];
T=[t(1) 1 1/t(1);t(2) 1 1/t(2);t(3) 1 1/t(3);t(4) 1 1/t(4);t(5) 1 1/t(5); t(6) 1 1/t(6)];
H_301=T\ENC_301;
H_315_0=T\ENC_315_0;
H_315_45=T\ENC_315_45;
H_315_90=T\ENC_315_90;

tau=0.1:0.1:16;

ENC_301_fit=sqrt(H_301(3)*(tau).^-1+H_301(2));
ENC_301_WSN=sqrt(H_301(3)*(tau).^-1);
ENC_301_WPN=sqrt(H_301(1)*tau);
ENC_301_pink(1:160)=sqrt(H_301(2));

ENC_315_0_fit=sqrt(H_315_0(3)*(tau).^-1+H_315_0(2)+H_315_0(1)*tau);
ENC_315_0_WSN=sqrt(H_315_0(3)*(tau).^-1);
ENC_315_0_WPN=sqrt(H_315_0(1)*tau);
ENC_315_0_pink(1:160)=sqrt(H_315_0(2));

ENC_315_45_fit=sqrt(H_315_45(3)*(tau).^-1+H_315_45(2)+H_315_45(1)*tau);
ENC_315_45_WSN=sqrt(H_315_45(3)*(tau).^-1);
ENC_315_45_WPN=sqrt(H_315_45(1)*tau);
ENC_315_45_pink(1:160)=sqrt(H_315_45(2));

ENC_315_90_fit=sqrt(H_315_90(3)*(tau).^-1+H_315_90(2)+H_315_90(1)*tau);
ENC_315_90_WSN=sqrt(H_315_90(3)*(tau).^-1);
ENC_315_90_WPN=sqrt(H_315_90(1)*tau);
ENC_315_90_pink(1:160)=sqrt(H_315_90(2));

figure(1)
loglog(tau, ENC_315_90_fit)
hold on
loglog(t,ENC_315_90_exp,'*')
```

```
loglog(tau,ENC_315_90_WSN,'-','Color','red')
loglog(tau,ENC_315_90_WPN,'-','Color','red')
loglog(tau,ENC_315_90_pink,'Color','red')
xlabel('Shaping Time (us)')
ylabel('ENC (e rms)')
title ('ENC vs Shaping Time S315@90V')
hold off
figure(2)
loglog(tau, ENC_315_0_fit)
hold on
loglog(t,ENC_315_0_exp,'*')
loglog(tau,ENC_315_0_WSN,'-','Color','red')
loglog(tau,ENC_315_0_WPN,'-','Color','red')
loglog(tau,ENC_315_0_pink,'Color','red')
xlabel('Shaping Time (us)')
ylabel('ENC (e rms)')
title ('ENC vs Shaping Time S315@0V')
hold off
figure(3)
loglog(tau, ENC_315_45_fit)
hold on
loglog(t,ENC_315_45_exp,'*')
loglog(tau,ENC_315_45_WSN,'-','Color','red')
loglog(tau,ENC_315_45_WPN,'-','Color','red')
loglog(tau,ENC_315_45_pink,'Color','red')
xlabel('Shaping Time (us)')
ylabel('ENC (e rms)')
title ('ENC vs Shaping Time S315@45V')
hold off

%Generating TXT file
ENCDetectr=[tau' ENC_315_0_fit' ENC_315_0_WSN' ENC_315_0_pink(1:160)' ENC_315_45_fit'
ENC_315_45_WSN' ENC_315_45_pink(1:160)' ENC_315_90_fit' ENC_315_90_WSN'
ENC_315_90_pink(1:160)'];
f = fopen('ENCDetector.txt', 'w');
fprintf(f, '%s\t%s\t%s\t%s\t%s\t%s\t%s\t%s\t%s\n','tau','ENC 0','ENC 0 WSN','ENC 0 pink','ENC
45','ENC 45 WSN','ENC 45 pink','ENC 90','ENC 90 WSN','ENC 90 pink');
for n = 1:160
   fprintf(f,'%.4f\t%.6f\t%.6f\t%.6f\t%.6f\t%.6f\t%.6f\t%.6f\t%.6f\t%.6f\n',ENCDetectr(n,:));
end
fclose(f);
```

APPENDIX C - BIPARAMETRIC CORRECTION SCHEME CODE

```
function outputfreqtable = frequencytable(ixd,iyd,handles)
global xi yi xr yr n xmin xmax ymin ymax
%Frequency Table code begining
if (get(handles.checkbox1,'Value') == get(handles.checkbox1,'Max'))
xi = linspace(min(ixd(:)),max(ixd(:)),n);
yi = linspace(min(iyd(:)),max(iyd(:)),n);
else
xi = linspace(xmin,xmax,n);
yi = linspace(ymin,ymax,n);
end
xr = interp1(xi,0.5:numel(xi)-0.5,ixd,'nearest',0.5)';
yr = interp1(yi,0.5:numel(yi)-0.5,iyd,'nearest',0.5)';
outputfreqtable = accumarray([yr' xr'] + 0.5, 1, [n n]);
%Frequency table code end
 % --- Executes on button press in pushbutton3.
function pushbutton3_Callback(hObject, eventdata, handles)
global xd yd xi yi cmax cmin contourlevels freq_table bpphbottom bpphtop bprtbottom bprttop bpn bpxd
bpyd
getvariables(handles);
PHdifference = bpphbottom - bpphtop;
bpyi = linspace(bprtbottom,bprttop,bpn);
bpxi = linspace(0,PHdifference,bpn);
bpyd=yd;
bpxd=xd;
for i=1:size(bpyd)
   if (bprtbottom<bpyd(i))&&(bpyd(i)<bprttop)&&(bpphtop<bpxd(i))&&(bpxd(i)<bpphbottom)
      bpbin=(bpyd(i)-bprtbottom)/((bprttop-bprtbottom)/bpn);
      bpbinround=ceil(bpbin);
      bpxd(i)=bpxd(i)+bpxi(bpbinround);
   end
end
freq_table = frequencytable(bpxd,bpyd,handles);
ax=handles.axes1;
hist(ax,xd,xi);
ax1=handles.axes2;
hist(ax1,bpxd,xi);
figure(1)
[C h] = contourf(xi, yi, freq_table, contourlevels);
set(h,'LineStyle','none');
caxis([cmin cmax])
colormap('hot')
% --- Executes on button press in pushbutton6.
function pushbutton6_Callback(hObject, eventdata, handles)
R=1;
%Reading the 4 points of the rectangle
ax=str2double(get(handles.edit16,'string'));
```

```
ay=str2double(get(handles.edit17,'string'));
bx=str2double(get(handles.edit18,'string'));
by=str2double(get(handles.edit19,'string'));
cx=str2double(get(handles.edit20,'string'));
cy=str2double(get(handles.edit21,'string'));
dx=str2double(get(handles.edit22,'string'));
dy=str2double(get(handles.edit23,'string'));
R=str2double(get(handles.edit24,'string'));
global xd yd xi yi cmax cmin contourlevels freq_table bpphbottom bpphtop bprtbottom bprttop bpn bpxd
bpyd
getvariables(handles);
bpphbottom=dx;
bpphtop=bx;
bprttop=by;
bprtbottom=ay;
PHdifference = bpphtop -bpphbottom ;
bpyi = linspace(bprtbottom,bprttop,bpn);
step1=(bprttop-bprtbottom)/(bpn-1);
bpxi = linspace(0,PHdifference,bpn);
%Lines Fuction
general_y=linspace(ay,cy,250);
step=(cy-ay)/(250-1);
%1st Line
m1=(dy-ay)/(dx-ax); %slope
b1=dy-m1*dx;%interception
Epoint=step*floor(dy/step)+ay;
x1=linspace(dx,ax,100);
y1=m1*x1+b1;
%2nd Line
m2=(cy-by)/(cx-bx); %slope
b2=cy-m2*cx;%interception
Epoint=step*floor(cy/step)+ay;
x2=linspace(cx,bx,100);
y2=m2*x2+b2;
%3rd Line
m3=(by-ay)/(bx-ax); %slope
b3=ay-m3*ax;%interception
Epoint=step*floor(bx/step)+ax;
x3=linspace(ax,bx,50);
y3=m3*x3+b3;
%4th Line
m4=(cy-dy)/(cx-dx); %slope
b4=cy-m4*cx;%interception
Epoint=step*floor(cy/step)+ay;
x4=linspace(cx,dx,100);
y4=m4*x4+b4;
k=0;
bpyd=yd;
bpxd=xd;
aux1=xd;
aux2=yd;
max=0;
for i=1:size(bpyd)
       flag1=0;flag2=0;
    if ((aux2(i)>ay)&&(aux2(i)<cy))
      if((aux1(i)>dx)&&(aux1(i)<bx))
```

```
        if (aux1(i)==ax)
           flag1=1;
        else
           slope=(ay-aux2(i))/(ax-aux1(i));
           if (aux1(i)<ax)
             if (slope<=m1)
                flag1=1;
             end
           end
           if (aux1(i)>ax)
              if (slope>=m3)
                 flag1=1;
              end
           end
        end
        if(aux1(i)==cx)
           flag2=1;
        else
           slope=(cy-aux2(i))/(cx-aux1(i));
           if (aux1(i)<cx)
              if(slope>=m4)
                 flag2=1;
              end
           end
           if (aux1(i)>cx)
              if (slope <= m2)
                 flag2=1;
              end
           end
        end
     end
  end
  if ((flag1==1)&&(flag2==1))
        k=k+1;
        %Middle point of line CD
        p2x=(cx+dx)/2;
        p2y=(cy+dy)/2;
        %Middle point of line AB
        p1x=(ax+bx)/2;
        p1y=(ay+by)/2;
        %Middle line Slope
        ms=(p2y-p1y)/(p2x-p1x);
        %Distance between a point and line of middle points
        d6=abs((p2x-p1x)*(p1y-bpyd(i))-(p1x-bpxd(i))*(p2y-p1y))/(sqrt((p2x-p1x)^2+(p2y-p1y)^2));
        d7(k)=abs((dx-ax)*(ay-bpyd(i))-(ax-bpxd(i))*(dy-ay))/sqrt((dx-ax)^2+(dy-ay)^2);
        if (d7(k)>max)
           max=d7(k);
        end
        theta=atand(ms);
        d8=d6*cos(90-theta);
        %Finding on which region is the the point
        middle_slope=(p2y-p1y)/(p2x-p1x);
        point_slope=(p1y-bpyd(i))/(p1x-bpxd(i));
        if (bpxd(i)>=p1x)
           position=1;
        else
```

```
            if(bpyd(i)<=p1y)
               position=0;
            else
               if (point_slope>=middle_slope)
                  position=0;
               else
                  position=1;
               end
            end
         end
         if(position==1)
            bpxd(i)=((bx+ax)/2)-d8;
         end
         if(position==0)
            bpxd(i)=((bx+ax)/2)+d8;
         end
%           bpxd(i)=ax-d8;
   end
end
freq_table = frequencytable(xd,yd,handles);
figure(1)
[C h] = contourf(xi, yi, freq_table, contourlevels);
set(h,'LineStyle','none');
caxis([cmin cmax])
colormap('hot')
hold on
plot(x1,y1,'yellow')
plot(x2,y2,'yellow')
plot(x3,y3,'yellow')
plot(x4,y4,'yellow')
hold off
max
freq_table = frequencytable(bpxd,bpyd,handles);
ax1=handles.axes1;
hist(ax1,xd,xi);
ax2=handles.axes2;
hist(ax2,bpxd,xi);
figure(3)
[C h] = contourf(xi, yi, freq_table, contourlevels);
set(h,'LineStyle','none');
caxis([cmin cmax])
colormap('hot')
```